

# Using the XMM-Newton Small Window Mode to investigate systematic uncertainties in the particle background of X-ray CCD detectors

Gerrit Schellenberger<sup>a,\*</sup>, Ralph Kraft<sup>a</sup>, Paul Nulsen<sup>a,b</sup>, Eric D. Miller<sup>c</sup>, Marshall W. Bautz<sup>c</sup>, Catherine E. Grant<sup>c</sup>, Dan Wilkins<sup>d</sup>, Steven Allen<sup>d,e,f</sup>, Silvano Molendi<sup>g</sup>, David N. Burrows<sup>h</sup>, Abraham D. Falcone<sup>h</sup>, Valentina Fioretti<sup>i</sup>, Richard F. Foster<sup>c</sup>, David Hall<sup>j</sup>, Michael W. J. Hubbard<sup>j</sup>, Emanuele Perinati<sup>k</sup>, Artem Poliszczuk<sup>d</sup>, Arne Rau<sup>l</sup>, Arnab Sarkar<sup>c</sup>, Benjamin Schneider<sup>c</sup>

<sup>a</sup>Center for Astrophysics | Harvard & Smithsonian, 60 Garden St., Cambridge, MA 02138, USA

<sup>b</sup>ICRAR, University of Western Australia, 35 Stirling Hwy, Crawley, WA 6009, Australia

<sup>c</sup>MIT Kavli Institute for Astrophysics and Space Research, 77 Massachusetts Avenue, Cambridge, MA 02139, USA

<sup>d</sup>Kavli Institute for Particle Astrophysics and Cosmology, Stanford University, 452 Lomita Mall, Stanford, CA 94305, USA

<sup>e</sup>Department of Physics, Stanford University, 382 Via Pueblo Mall, Stanford, CA 94305, USA

<sup>f</sup>SLAC National Accelerator Laboratory, 2575 Sand Hill Road, Menlo Park, CA 94025, USA

<sup>g</sup>INAF - IASF Milano, Via A. Corti 12, 20133 Milano, Italy

<sup>h</sup>Pennsylvania State University, Department of Astronomy and Astrophysics, University Park, Pennsylvania, United States

<sup>i</sup>INAF Osservatorio di Astrofisica e Scienza dello Spazio di Bologna, Bologna, Italy

<sup>j</sup>The Open University, Centre for Electronic Imaging, Milton Keynes, United Kingdom

<sup>k</sup>Institut für Astronomie und Astrophysik, Eberhard Karls Universität Tübingen, 72076 Tübingen, Germany

<sup>l</sup>Max Planck Institute for Extraterrestrial Physics, Giessenbachstrasse 1, 85748 Garching, Germany

**Abstract.** The level and uncertainty of the particle induced background in CCD detectors plays a crucial role for future X-ray instruments, such as the Wide Field Imager (WFI) onboard Athena. To mitigate the background systematic uncertainties, which will limit the Athena science goals, we aim to understand the relationship between the energetic charged particles interacting in the detector and satellite, and the instrumental science background to an unprecedented level. In addition, we characterize the temporal variability of the instrumental background from minutes to years. These particles produce easily identified “cosmic-ray tracks” along with less easily identified signals produced by secondary particles, e.g., X-rays generated by particle interactions with the instrument and indistinguishable from genuine sky X-rays. We utilize the Small Window Mode of the PN camera onboard XMM-Newton to understand the time, spatial and energy dependence of the various background components, particularly the particle induced background. While the distribution of particle events follows expected detector readout patterns, we find a particle track length distribution inconsistent with the simple, isotropic model. We also find that the detector mode-specific readout results in a shifted Cu fluorescent line. We illustrate that on long timescales the variability of the particle background correlates well with the solar cycle. This 20-year lightcurve, can be reproduced by a particle detector onboard Chandra, the HRC anti-coincidence shield. We conclude that the self-anti-coincidence method of removing X-ray-like events near detected particle tracks in the same frame can be optimized with the inclusion of additional information, such as the energy of the X-ray. The results presented here are relevant for any future pixelated X-ray imaging detector, and could allow the WFI and similar instruments to probe to truly faint X-ray surface brightness.

**Keywords:** Sun; particle emission; X-rays; diffuse background; cosmic rays; instrumentation; detectors.

\* [gerrit.schellenberger@cfa.harvard.edu](mailto:gerrit.schellenberger@cfa.harvard.edu)

## 1 Introduction

Many science goals carried by instruments of future X-ray observatories, such as the Wide Field Imager (WFI)<sup>1–3</sup> onboard Athena, are driven by the detection and modeling of faint, diffuse sources,

such as galaxy cluster outskirts. While measurements with current X-ray observatories are often limited by photon statistics, observatories with large collecting areas will mostly be impacted by systematic uncertainties. As shown, e.g., by 4, the systematics of the background, especially the non-X-ray background (NXB), limit the feasibility of measurements on cluster outskirts, independent of the statistical significance of the measurement: Once the signal is below the background, longer observing times cannot make up for the level of uncertainty in the background modeling. This is not unique to cluster outskirts, but applies to any faint source, such as, distant black holes, or detecting the first galaxy clusters and groups, both major science drivers of Athena/WFI.<sup>1,5,6</sup> Therefore, the level and properties of the background produced by high-energy galactic cosmic ray (GCR) particles plays a crucial role in the design of future X-ray observatories.

We classify the NXB as any feature read out by the detector, that is unrelated to sky X-rays focused by the telescope, such as GCRs.<sup>7</sup> We can broadly divide the particle interactions into primary interactions of the (mostly) GeV protons with the detector, and events from secondary particles. The former leave “tracks” in the detector that are easily identifiable, and are typically removed during onboard processing, while the latter are electrons or fluorescent X-rays caused by GCRs interacting with the housing and other material surrounding the detector. Soft protons emitted by the sun would also fall under the NXB definition, but are unrelated to GCRs and can be filtered out, e.g., with a magnetic diverter,<sup>8–11</sup> or a thick layer of aluminum (closed filter position, 12).

While the primary GCR interactions deposit a charge signature that is very characteristic, both in terms of amplitude and pattern distribution, the events from secondaries, however, can mimic the energy and pattern of sky X-rays and, so, constitute the major component of NXB in X-ray observations. This NXB typically starts to dominate over other background components (e.g., the Galactic foreground emission, and X-ray emission of unresolved point sources) above 2 keV. Any mitigation of the NXB through simple background subtraction or modeling is problematic since the NXB is variable spatially, in energy and in time. Additionally, detectors such as the XMM-Newton PN also have a significant noise contribution from electronic readout artifacts<sup>13</sup> below  $\sim 300$  eV.

As part of a larger effort within the Athena WFI Background working group (see also 14–19) we aim to characterize the NXB by utilizing the Small Window Mode (SWM) of the European Photon Imaging Camera PN detector onboard XMM-Newton. This enables us to understand the time, spatial and energy dependence of the particle induced background component, which is critical to verify cosmic ray simulations with Geant4. Its similarity to the Athena/WFI in terms of pixels size, a short frame time, and the availability of all (normally rejected background) events, makes the XMM-Newton PN SWM a unique tool for these studies. While typically used for observations of bright point sources, such as quasars, XMM-Newton archive also hosts a wealth of data taken in SWM between science observations, when the satellite was slewing to the next target. These several hundred exposures, each a few kiloseconds long, are ideal for background investigations due to the lack of a bright science target near the center of the field. While in a previous study, 15 investigated a similar dataset in the limited energy band from (2 – 7) keV, a lot more information can be extracted by, a) utilizing the full energy band, b) including more observations in various filter configurations, and c) comparing these data with data from other instruments, such as the Chandra High Resolution Camera (HRC) anti-coincidence shield rates.

Our goal is to reach a better understanding of the GCR induced background in X-ray CCD observations to both, lower the level of this particle background, and limit the systematic uncertainties connected with it. The latter is required so techniques that account for the background in

X-ray observations become more reliable (e.g., background subtraction), due to its variable nature. PN allows observations in SWM, that operates a small area of the detector (about 3% of the total area), but does not apply onboard minimum ionizing particle (MIP) thresholding, i.e., all events processed are retained in the final event file. Self anti-coincidence (SAC) is an important tool to mitigate the particle induced background, and therefore illustrate and optimize the methodology. 18 demonstrated through detailed Geant4 simulations the prospects of Geant4 for the Athena WFI. While many of our results feed into the application of SAC, it is not the only focus of this study. We want to emphasize that only a thorough understanding of all manifestations of the particle background allows us to develop algorithms that reduce the systematic uncertainties in X-ray observations. SAC is one way of directly lowering the background, but the knowledge of the time variability of particles for example, greatly helps to develop or adjust algorithms that rely on the precise particle background level.

In Section 2 we describe our XMM-Newton and Chandra HRC data reduction and analysis procedure. Section 3 explores the spatial, spectral and temporal characteristics of the NXB components, and compares the time variability of primaries and secondaries with the Chandra HRC shield. Section 4 links the previous results with an optimized self-anti coincidence filtering method, which enables a significant reduction of the background level, especially for detectors like the Athena/WFI. We summarize our findings in Section 5.

## 2 Data and Analysis

### 2.1 XMM-Newton PN

#### 2.1.1 Data selection

The PN SWM only reads an array of 64x63 pixels on CCD 4 of PN, and is our operating mode of choice to trace particle interactions with the detector. It also operates with a short frame time of 5.6718 ms, and the PN has a pixel size of 150  $\mu\text{m}$ .<sup>20</sup> Both values are similar to those expected for the Athena WFI.<sup>2</sup> A large number of relatively short (typically few ks) PN SWM observations were taken during slews between science target observations. In many cases the filter wheel was in the closed position (FWC) for these slew observations in SWM, making them ideal to study only particle interactions with the detector, with no celestial X-rays hitting the detector.

The archival PN SWM slew observations start in the year 2002, and span over 20 years. On average 97 ks per year of data are taken in SWM slews, of which 80% are the FWC observations that are particularly useful for our study. We process a total of 665 SWM observations, including the 308 analyzed in 15.

Lastly, slew observations in full frame mode (FF) include none of the detailed information on particle interactions kept for SWM, but they can be combined with the knowledge gained from SWM on the particle background to provide a better understanding of soft proton flares (e.g., 21, and section 3.4). We analyzed 2666 FF observations from slews, which add to a total livetime of 7.4 Ms. This dataset is unique as the slew mode provides an average sky exposure for every observation, and even slews across bright sources in the sky will not bias the overall measurement.

#### 2.1.2 Data processing

We process the raw XMM-Newton PN data using the Science Analysis Software (SAS,<sup>22</sup> version 21), and incorporate some non-standard parameters and tasks. We illustrate our processing pipeline

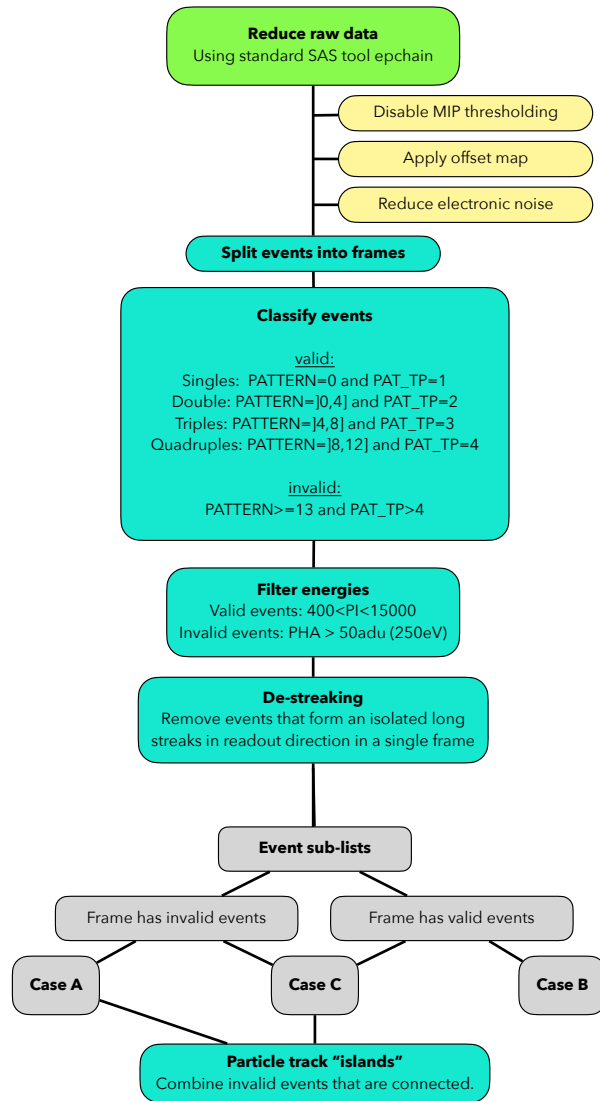


**Fig 1** Illustration of the processing of the XMM-Newton PN Small Window Mode Slew datasets to separate particle-track-only frames (Case A), Sky X-ray events (Case B), and mixed frames (Case C).

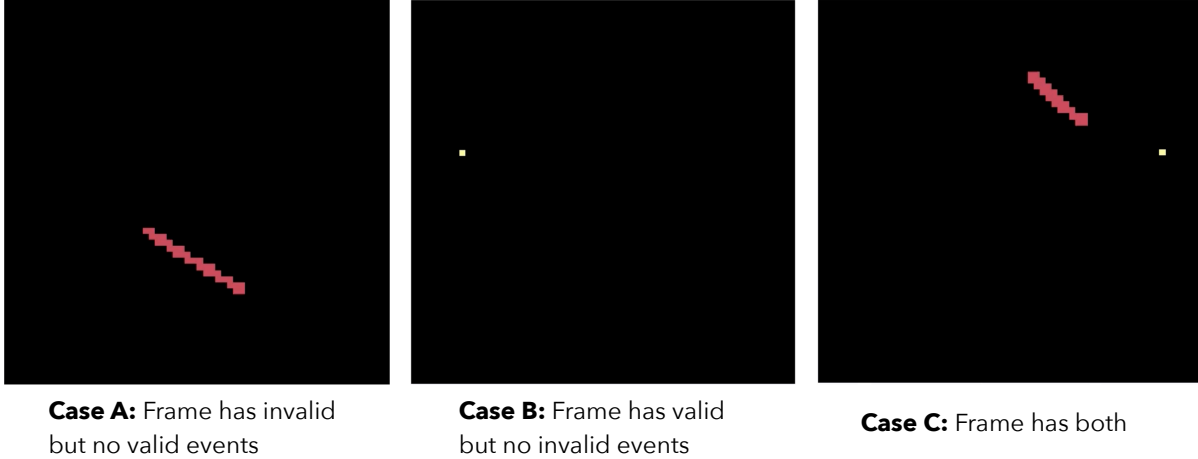


**Fig 2** Examples for the different frame types in the PN/SWM data that contain either valid events (yellow), or invalid events (red). The black box marks the active pixel region.

in Fig. 1. First, we download the Observation/Slew Data Files (ODF/SDF) from the XMM-Newton archive server, and process it using the Current Calibration Files (CCF) from 2023-11-01. We follow the default steps using the standard SAS tasks, including `cifbuild`, and `odfingest`. To create the event list with `epchain`, we apply the parameter `anmip=4095`, to disable the MIP thresholding and include all particle events in the output event file. Offset maps are typically used to subtract the energy offset for each pixel. However, slew observations do not take offset maps before the exposure, and we make use of the `runeproject` algorithm<sup>13</sup> to resolve this issue. We also apply the `epnoise` algorithm,<sup>13</sup> which removes frames that are dominated by electronic noise below 150 eV.

To not introduce any biases in our analysis, we turned off the randomization and badpixel detection algorithms. The processed fits file contains an extension with the resulting event list (HDU 1), and a further extension containing a list of all the frames with corresponding timestamps (HDU 4). We found a total of 665 SWM slew observations in the archive made up to the end of November 2023, 519 with the filter in the closed position, 139 with the medium optical blocking filter, and 7 with the FWC and the onboard calibration source (calclosed). In the following we exclude observations with a very high radiation environment: The median Advanced Composition Explorer (ACE) EPAM proton flux (112–187 keV) has to be below  $2450 \text{ proton s}^{-1} \text{ cm}^{-2} \text{ sr}^{-1} \text{ MeV}^{-1}$ . This excludes 32 FWC and 7 medium filter observations taken during time periods with high solar activity.

The remaining 626 slew observations consist of a total of 355 495 332 frames, summing to more than 2 Ms of observing time, with 5 028 119 frames (1.4%) containing events. We list all observations in Tab. 1. We then classify the events as valid or invalid, based on the energy and pattern: valid events have either a single, double, triple, or quadruple charge pattern distribution based on the [SAS classification](#). Any event with a pattern larger than quadruple (`PAT_TYP > 4` and `PATTERN ≥ 13`) is classified as invalid. We further filter the valid and invalid events in energy or pulse height amplitude (PHA), where valid events are required to have an energy (PI column) between 400 and 15 000 eV, and the invalid events need to have a PHA of at least 50 adu, equal to approximately 250 eV (see Fig. 1 for an overview of the processing). However, each frame

with invalid events must at least contain one event with energy of more than 16 keV, indicating a MIP. Otherwise the frame is discarded. We noticed that in some frames a number of invalid events are arranged in a line following the readout direction. This happens more often than expected for the rare case of perfectly aligned particle tracks, and these detections are likely due to artifacts from the readout. We remove these events from our final event list whenever the length of the streak is at least 5 pixels in the readout direction, and no events are detected in adjacent columns. We note that since readout streaks can appear in consecutive frames, we apply the method above to the combination of two consecutive frames, which has twice the number of rows of a single frame. In total we find that 3 935 200 frames have only invalid events (Case A frames, 1.1 %), 1 045 910 frames have only valid events (Case B frames, 0.3 %), and 47 009 frames have both, valid and invalid events (Case C frames, 0.01 %). The vast majority (99.94%) of all Case A frames contain more than two or more invalid events. We illustrate the different frame types in Fig. 2. Invalid events are mostly caused by GCRs passing through the detector and depositing charge in connected pixels. These particle tracks can be further classified using a simple segmentation algorithm that outputs the energy weighted centroid, the total energy and number of pixels in the particle track. We confirmed that the majority ( $> 97\%$ ) of the particle tracks are well approximated by a rectangular box, with two or less pixels deviations.

## 2.2 Chandra High Resolution Camera

HRC is one of the two focal plane instruments onboard Chandra.<sup>23</sup> The HRC consists of microchannel plates to detect X-rays, and is surrounded on 5 sides by a plastic scintillator, with photomultiplier tubes (PMTs) as detectors, that serves as an anti-coincidence shield to reduce the background from energetic particles.<sup>24</sup> In order to detect high levels of solar particle fluxes that could be harmful for the instruments onboard Chandra, the HRC shield also records data when the HRC instrument is not in the focus. However, since late 2020 the shield is no longer operated when the HRC is not actively observing. The recorded shield rates are several 1000 counts per second, recorded at 32.8 s time intervals. This implies a negligible statistical uncertainty at minute-length time bins, while it has continuous records of the particle environment since the beginning of the Chandra mission (except for radiation zone passages lasting about 12 hours, and a few spacecraft safing events, losing about 17% of time) until 2020. The HRC shield count rates constitute one of the most valuable datasets to analyze the evolution and correlation of particles that induce the non-X-ray background.

We retrieved the data from the Chandra X-ray Center, and applied a median filter to clip very high values that are due to corruption of the secondary science data.

## 3 Characterizing the nature of the particle background

Systematic uncertainties arising from the unpredictability of the NXB in X-ray observations can bias, and therefore limit, the science goals<sup>25</sup>. While energetic particles that interact with the detector produce the easily identifiable “cosmic-ray tracks”, secondary X-ray-like events are difficult to identify and remove. Such secondaries often produce identical signals to the X-rays focused by the optics and traditional filtering algorithms cannot reliably remove them. We develop and optimize algorithms and methods to remove these secondary X-ray-like events, which is strongly dependent on the accurate knowledge of the temporal, spatial, and spectral variation and distribution of



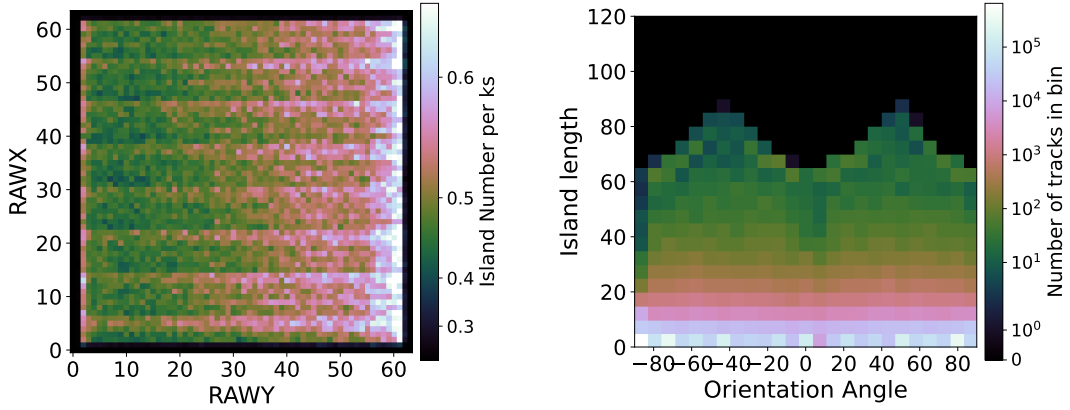


**Fig 3** Left: Average number of the particle tracks (islands) as a function of their centroid distribution. The colorscale is in units of island centers in each pixel per ks. Right: Histogram of the island orientation and length distribution. The colorscale shows the number of islands in each bin.

both, the signatures of primary interactions (particle tracks) as well as the X-ray-like events from secondaries.

### 3.1 Spatial distribution of particle tracks in the FWC slew data

In order to understand the distribution of particle tracks, which consist of invalid events, we define event islands, where all invalid events are merged into a single shape as long as they are not separated by more than  $\sqrt{2}$  pixel. These islands are characterized by a centroid, a major and minor axis, and the rotation angle (orientation). Therefore, a single frame can have more than one island, if the closest separation is more than  $\sqrt{2}$  pixel. We employ a simple segmentation algorithm [26, Chapter 2] that provides these island parameters. We investigate the distribution properties in the following.

The overall distribution of islands across the detector is best parametrized by the 2D distribution of island centroids (Fig. 3 left). The number of islands increases with increasing RAWY, which is the detector readout direction. The readout of PN in SWM can be separated into 4 steps: An initial fast shift of charges before the actual integration (“clear the window”), the integration, a second fast shift to move the charges to the readout area, and the “slow” readout. Each of these steps adds a row-dependent exposure time until the charge is read out. The first step adds 720 ns to the row with the highest RAWY, and 46  $\mu$ s for the lowest RAWY row. The second and thirds step expose all pixels uniformly, 4 ms in step 2 and 0.1 ms in step 3. Step 4 shifts charges with 1 row per 23  $\mu$ s, so the highest RAWY row has an additional 1.5 ms exposure. Adding up these 4 steps, we expect 34.6% more events in the highest RAWY row compared to the lowest RAWY row. For more details see 27 and the [XMM User Handbook](#), Issue 2.21, Section 3.3.10. This is consistent with the increasing trend of islands in RAWY direction (Fig. 3 left), where we find 33% if we exclude the edge pixels. For the columns (RAWX direction) we do not find a linear trend across the detector, as expected. However, we see a slight edge or increase in counts in regular intervals due to the different CAMEX readout electronics, and the associated variations in amplification. In Case C frames we find a very similar pattern (with less statistical significance). However, a much larger fraction of the Case C frames are caused by fluorescent X-rays, when a GCR hits the

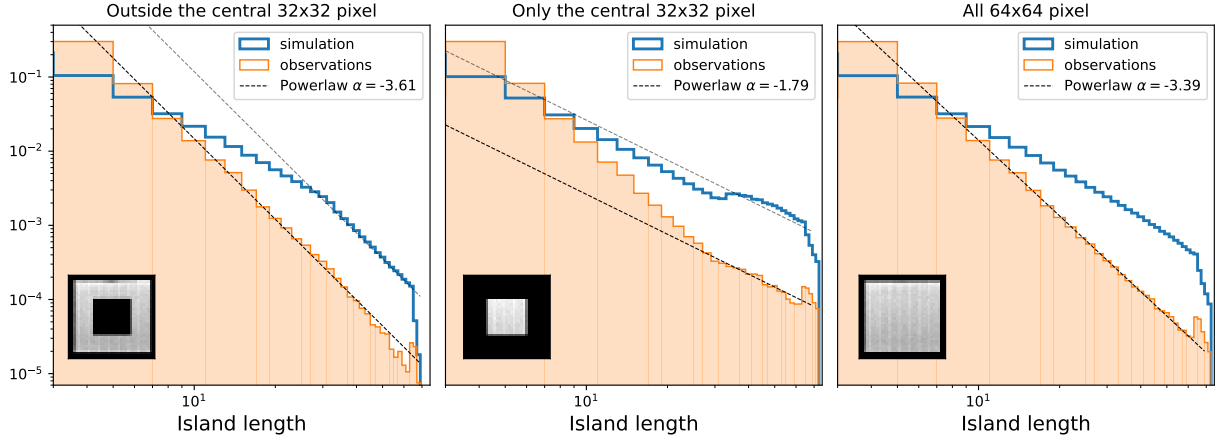


**Fig 4** Island length distribution (in pixel) for three apertures: Tracks with the centroid located in the central 32x32 pixels (middle panel), outside the 32x32 pixels (left panel) or anywhere on the detector (right panel). Note that these apertures only refer to the location of the island centroid, and do not necessarily exclude invalid events in the outer or inner region. The apertures are shown in small insets at the bottom left of each panel. The measured distributions are shown by filled orange bars, the distributions from simple simulations in blue, and a powerlaw fit to the longer track distributions as black dashed lines.

electronics board and triggers a fluorescent Cu/Zn photon. This mainly occurs during the readout and not during the exposure/integration phase, since most of the Small Window is located at the Cu hole in the board. Therefore, the trend is expected to be even steeper for Case C frames, which is indeed what we find (156% increase).

The island orientation angle features no spatial dependence, and the overall distribution of angles is fairly uniform, with several peaks at values corresponding to 90 or 45 deg. Similarly, the spatial distribution of island lengths is also fairly uniform across the detector. However, we notice a cross-like features in the middle of the detector. This can be explained with the centroids of the longest tracks having to be located in the center of the detector. The distribution of island length and orientation angle is shown in Fig. 3 (right). While it is clear that longer tracks are less common independently of the angle, we notice two peaks at  $-45$  and  $+45$  degree and length longer than 64 pixels. The detector geometry (64x63 pixels) requires that any longer tracks must have angles other close to  $\pm 45$  degree.

When we look at the overall distribution of track lengths we find that it can be approximated by a powerlaw distribution with index  $-3.4$  (see orange bars Fig. 4, right panel). In order to isolate any edge effects we also look at two other apertures, the central 32x32 pixel, and the region outside the central 32x32 pixel. Note that these apertures only refer to the location of the island centroid, and do not necessarily exclude invalid events in the outer or inner region.

Orange bars show the length distribution of the three apertures in Fig. 4. We compare these distributions with a simple three dimensional box model of the detector, where we randomly assign particle tracks. We ensure that the simulated particle flux through all the sides of the box model is conserved, and the angular distribution of the particle vector is uniform, i.e., an isotropic particle field. We then measure the projected length distribution, which is shown in Fig. 4 as blue lines. We find in the central 32x32 pixel area (Fig. 4 middle panel) the slope of the longer tracks ( $\geq 30$  pix) matches the simulated distribution (slope of about  $-1.8$ ). However, there is steeper trend for



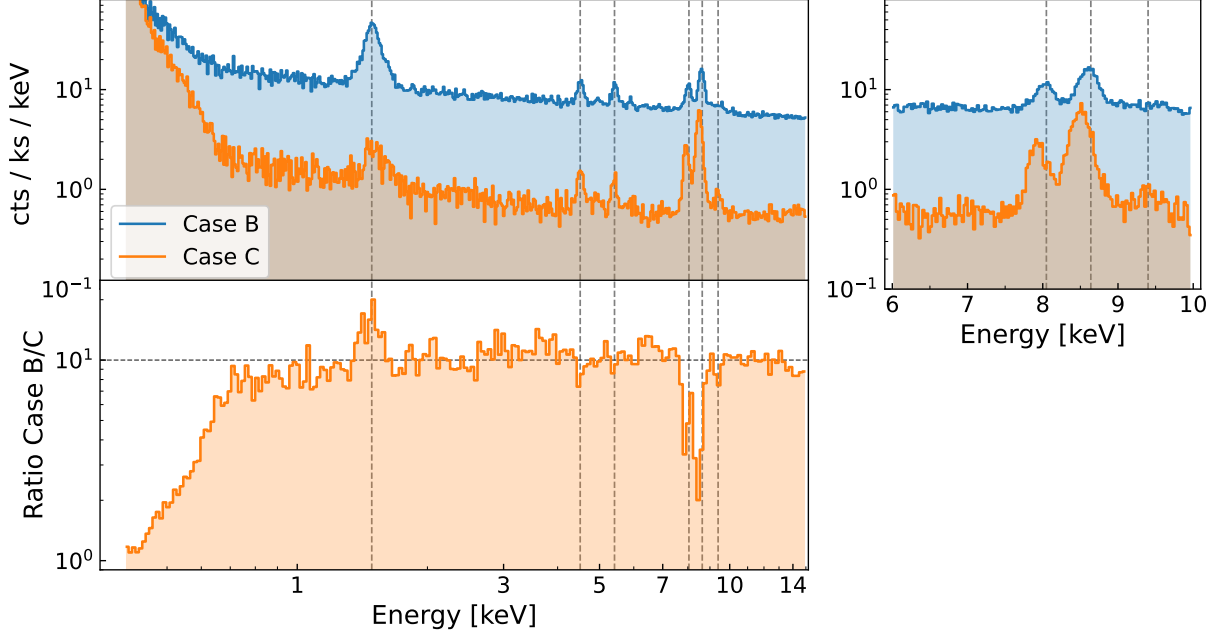


**Fig 5** Top: Spectrum of valid events in Case B (blue) and Case C (orange) frames. The vertical dashed lines correspond to the spectral lines Al  $K\alpha_1$  (1.487 keV), Ti  $K\alpha_1$  (4.511 keV), Cr  $K\alpha_1$  (5.415 keV), Cu  $K\alpha_1$  (8.048 keV), Zn  $K\alpha_1$  (8.639 keV), and Pt  $L\alpha$  (9.4 keV). Bottom: Ratio of the Case B/C spectra to highlight differences in line strengths.

shorter tracks, meaning we observe more short tracks than expected from a simple model.

For short-length islands none of the simulated cases (full detector, central part of detector, without central part of detector) can reproduce our observations. For the detector events excluding the central 32x32 pixels (Fig. 4 left) we find a much steeper slope of  $-3.6$ , while the simulations predict a flattening at the shorter track lengths. For longer island ( $> 25$  pixels) we find comparable slopes in Fig. 4 left and middle. We can only speculate that the excess of shorter islands is caused by a different population of particles, or secondaries in the same frame, or our detector model and isotropic particle flux assumption is not applicable for these types of particle interactions. In the future we plan to perform detailed Geant4 simulations with an accurate PN mass model to understand the length distribution.

### 3.2 Spectral properties of particle background components

We analyze the energy distribution of valid events in Case B and C frames in the PN SWM dataset with filter closed position. Figure 5 shows the spectrum of Case B (blue) and Case C (orange) valid events. The spectrum has a slowly declining continuum, with 5 clearly identified emission lines: Al  $K\alpha_1$  (1.487 keV), Ti  $K\alpha_1$  (4.511 keV), Cr  $K\alpha_1$  (5.415 keV), Cu  $K\alpha_1$  (8.048 keV), Zn  $K\alpha_1$  (8.639 keV). We also see a hint of Pt  $L\alpha$  (9.4 keV) in the Case C frames, which does not show up in the Case B frames, despite better statistics. Overall, the continuum part of the spectrum above 0.8 keV is very similar between Case B and C frames (apart from the obvious difference in normalization due to the count rate, see bottom panel in Fig. 5).

At the soft end below 0.6 keV we see a steep increase which mostly comes from electronic noise.<sup>28-31</sup> It appears even steeper for Case C valid events. In Fig. 6 we find that the low energy

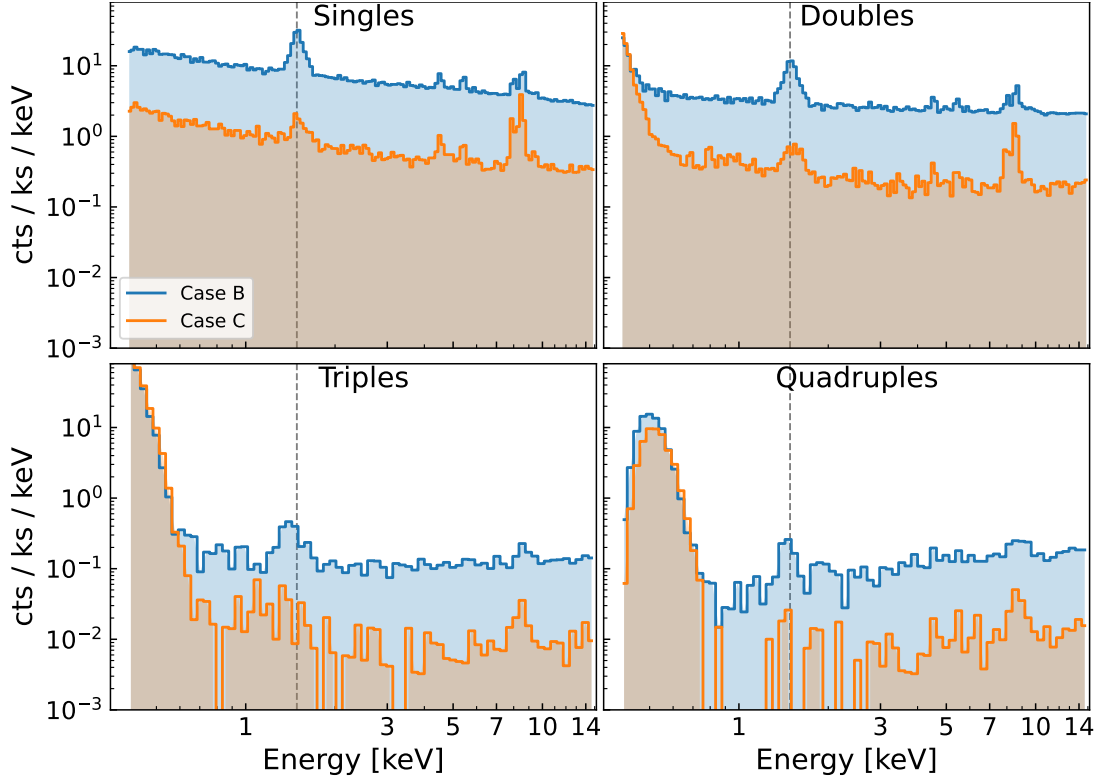


**Fig 6** Spectra of valid events in Case B (blue) and Case C (orange) frames split by the event pattern distribution.

noise becomes more and more dominant (and shifted toward higher energies) for event patterns showing more pixels above threshold, and single events are largely unaffected.

Another striking difference between the Case B and C valid events is the shift of the Cu and Zn fluorescent lines toward slightly lower energies in Case C frames (see Fig. 5 right panel). This is independent of the pattern, however triples and quadruples have poor statistics to resolve the line energies. If we look at the difference of the Case C Cu and Zn line energies from their nominal values over the lifetime of the mission, we find the the difference was largest early in the mission (up to 150 eV in 2007) and continuously decreased to about 70 eV in 2020. The PN circuit board underneath the detector has no Cu or Zn in the central region (“copper hole”, see 31, 32), which is the location of the SWM aperture. Therefore, Cu fluorescent X-ray events are very unlikely to deposit charge in the active detector region during integration. During the readout phase a fluorescent Cu or Zn photon produced by a GCR adjacent to the shifted charge region is much more likely to be detected. This also explains why these two fluorescent lines are so much brighter in Case C than in Case B frames (relative to the continuum). The few fluorescent Cu and Zn photons in Case B frames are likely produced during the integration phase from a GCR that misses the aperture, while the fluorescent photon scatters into it. During readout however, the GCRs can easily produce fluorescent Cu and Zn photons that are detected, but end up in a frame with a particle track, as Case C frames. The readout is likely going to affect the detected photon energy, which systematically shifts these lines in Case C frames. For Case C frames with a Cu/Zn X-ray the single pattern fraction is much higher than for Case B Cu/Zn photons (73.9% vs. 60.5%, with 1.6% and 1.0% statistical uncertainty, respectively). This might explain the shift toward lower energies of the Cu/Zn lines in Case Cs: The Cu layer is physically very close to the detector, and

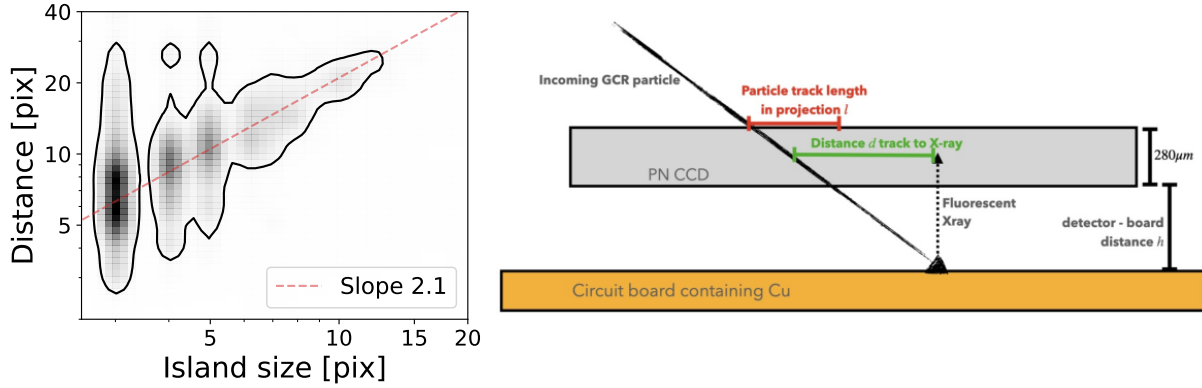


**Fig 7** Left: Fluorescent Cu X-rays in Case C frames show a correlation between the length of the associated particle track in the frame  $l$ , and the distance between X-rays and track. Right: Illustration showing the path of a GCR through the detector, leaving a track (red), and triggering the emission of a Cu X-ray from the circuit board underneath. The distance between the board and the CCD  $h$  can be derived with simple geometric assumption.

fluorescent photons will therefore be also close to any particle track. If the charge in the detector from the Cu/Zn photons is split over multiple pixels (pattern), some of it might be confused with the nearby particle track and is not correctly added to the X-ray-like event. This will reduce the charge in Case Cs, but not in Case Bs, which do not contain a particle track.

In order to verify our picture of the Case C fluorescent Cu events, we look at these events in a bit more detail: From the 775 Case C frames with a valid event energy consistent with Cu, we correlate the particle track length with the distance between the track and the X-ray event in each frame. We compare the smoothed distribution with a slope 2.1 in Fig. 7 (left). The larger the angle of the incoming GCR, the longer the track and the further we expect the fluorescent X-ray to be detected from the GCR detection. We illustrate the geometry in Fig. 7 (right), where one can easily conclude the following identity:

$$h = 280 \mu\text{m} \frac{d}{l}, \quad (1)$$

where  $\frac{d}{l}$  is the slope in Fig. 7 (left). We can therefore derive the separation between the detector and the board. We find a separation of about  $h \approx 2.1 \times 280 \mu\text{m} - 140 \mu\text{m} \approx 450 \mu\text{m}$ , which is a reasonable result considering that the actual distance is  $250 \mu\text{m}$  (33), and the pixel thickness (depletion depth) is  $280 \mu\text{m}$ .

### 3.3 Temporal variability of the particle background

The time variability on various scales remains a significant source of systematic uncertainty in the NXB (e.g., 30). A rapidly changing particle rate and/or spectrum will render any blank sky background subtraction very difficult, and likely insufficient for future missions such as Athena WFI, which require a precise knowledge of the background.<sup>2</sup> Instead a deeper understanding of the particle background variability and its dependencies is required to develop models and mitigation methods. In the following we analyze the lightcurves of the particle interactions with the PN and the Chandra HRC anti-coincidence shield. The latter has negligible statistical uncertainty and (almost) continuous sampling with extremely high time resolution for 20 years.

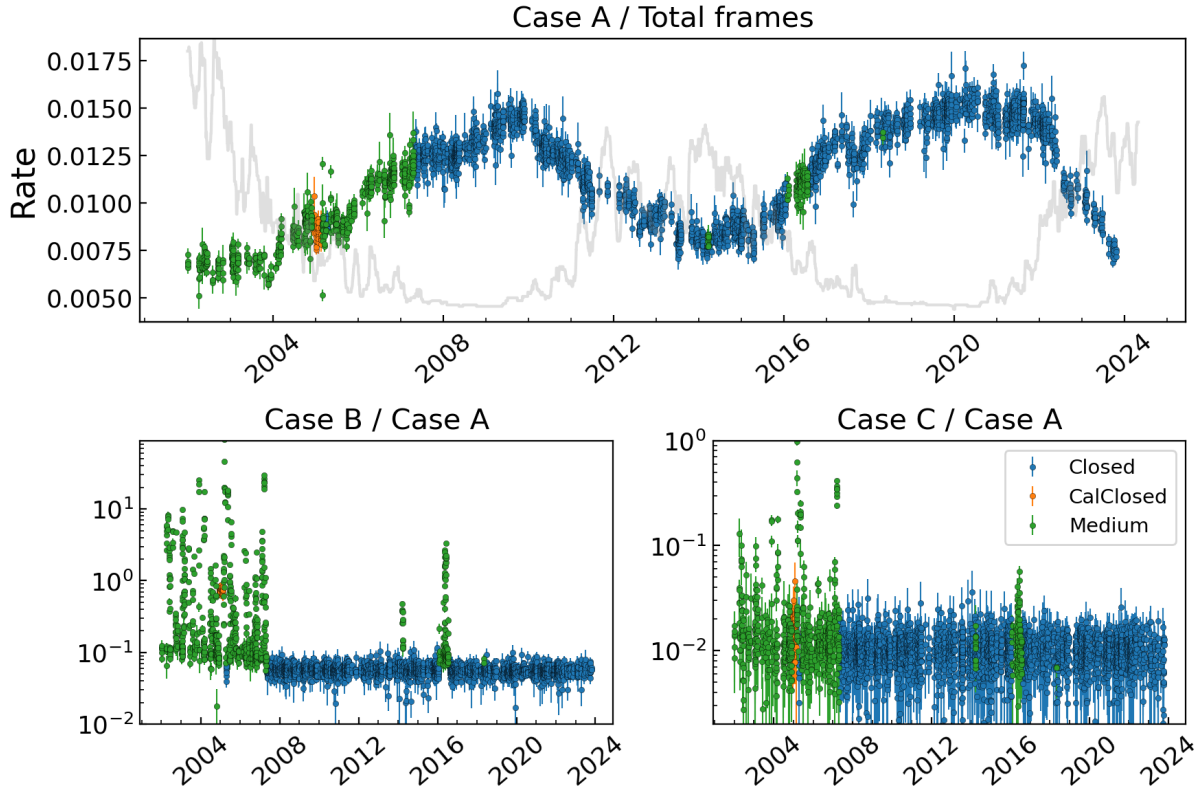


**Fig 8** Lightcurves of the PN SWM slow observations with 10 minute time resolution. Top: Case A (only invalid in frame) frame rate. We also show the average number of sunspots in grey (arbitrary y scale) as provided by WDC-SILSO, Royal Observatory of Belgium, Brussels. Bottom left: Ratio of Case B to Case A frame rate. Bottom right: Case C frames per Case A frame. The color in all panels refers to the filter position (closed: blue, open/medium: green, closed with calibration source: orange).

### 3.3.1 PN Small Window Mode

We select our previously analyzed slow observations in SWM, which have been taken either in FWC mode, medium filter, or CalClosed mode. On average we find that about 1 to 2 percent of all frames contain invalid events. Therefore, the chance of randomly detecting two independent GCRs in a single frame is  $< 0.04\%$ , and therefore negligible. The number of invalid events (i.e., the total number of pixels in particle tracks) is not a good measure for the particle background rate, as, depending on geometry, tracks appear longer and sometimes events from secondary particles are also detected. We can therefore assume that invalid events in the same frame are not independent. Also the number of islands/tracks is not a good measure of the primary particle rate, as a single primary can trigger a “shower” of secondary events which might be detected as invalid events in separate islands within the same frame (this happens in  $\sim 5\%$  of the Case A frames). Therefore, the best quantity to use is the number of frames with invalid events, as this is the least noisy tracer of the particle rate.

We calculate the rate of invalid events in 10 min time bins, with each bin having typically 1000 invalid frames (about  $3.2\%$  expected statistical uncertainty). We actually measure an RMS scatter from bin to bin of  $3.4\%$ , very close to our expectations, therefore, showing that on 10 min intervals the statistical uncertainty dominates over systematic changes within the same period. Figure 8 (top

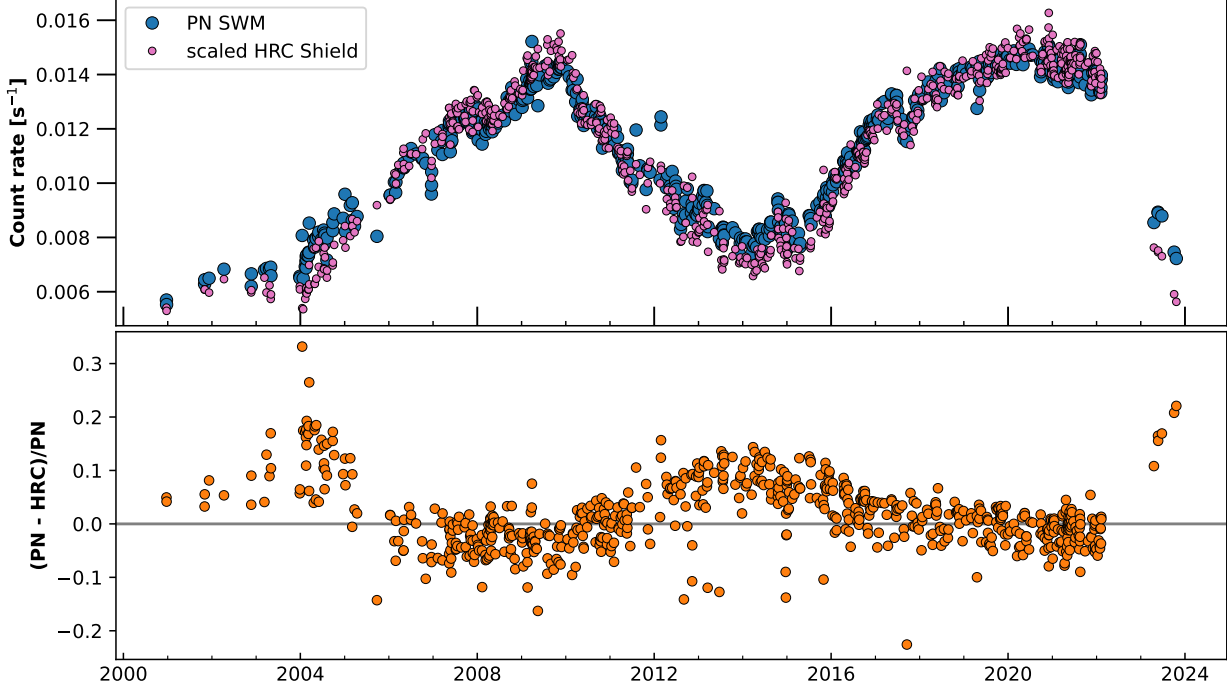


**Fig 9** Comparison of the Chandra HRC shield lightcurve and the XMM PN SWM Case A frame rates. Top panel: Direct comparison of the rates, where the HRC shield data (purple, typically several thousand counts per second) are rescaled by a constant factor to overplot with the much smaller, and also rescaled with a time dependent function to correct for the loss of PMT sensitivity. Bottom panel: Relative residuals between PN SWM Case A frames and HRC shield count rates.

panel) shows the Case A frame rate over more than 20 years (almost two full solar cycles). On timescales of years the lightcurve clearly follows the solar cycle, as initially suggested by 34. For comparison we overplot the number of sunspots in Fig. 8 (grey line in top panel), which anti-correlates with the particle background rate. The scatter in the Case A rates from closed and medium filter observations (blue and green points, respectively) is determined with respect to a smooth spline that we fit to the lightcurve. We find that FWC observations have a scatter of 4.8%, while medium filter observations have 5.3% scatter. However, the two sided KS-test shows that the two distributions, residuals from closed and medium filter observations, are the same (p-value 0.89). We can therefore conclude that we see no indications that the Case A frames, even for medium filter observations, are affected by sky X-rays. Case A frames trace the particle background level and any method that utilizes the particle tracks in Case A or C frames to estimate or mitigate the X-ray particle background can be applied to sky observations as well.

The Case B frames behave very differently. Figure 8 (bottom left panel) shows the Case B frame rate normalized by the Case A rate. For FWC observations (blue) the ratio is almost constant, showing that there is no other source of Case B events. For Medium filter observations (green) we find a higher baseline level due to celestial X-rays, and also over two orders of magnitude of scatter. For these variations to originate from bright X-ray sources that happen to lie on the slew path, they would need to be extremely bright: The XMM-Newton slew rate is about 90 deg per minute, which means that a source is only within the SWM aperture for about 4 seconds. The typical quiescent count in Case B frames is  $10^{-3}$ , which means about  $0.18 \text{ ct s}^{-1}$ , or 650 counts in a typical 1 h observation. Therefore, a bright source, which is visible for about 4 s, will have to

contribute about 64 000 cts in order to increase the overall count rate by two orders of magnitude. This means the source needs to have a flux of at least  $3 \times 10^{-8} \text{ erg s}^{-1} \text{ cm}^2$ , which is more than the Crab SNR. We can safely assume that XMM-Newton does not regularly slew across Crab-like sources, and exclude the possibility that celestial X-rays cause the spikes seen in medium filter slew observations. The only other explanation is soft protons, that get partly focused by the XMM optics and cause X-ray like patterns and energy signatures.<sup>35,36</sup> We verified this by analyzing over 2700 slew observations in PN Full Frame mode. The Case B frames can be easily identified in these observations, but unlike the SWM we are unable to measure the Case A frames. Since we know the trend with time from the SWM observations (Fig. 8 top panel), we can interpolate to obtain an approximate Case B/A ratio for FF observations. When comparing these rates with the values from the Fin/Fout test<sup>37</sup> we find consistency, meaning the same observation that are flagged as soft proton contaminated, have a high Case B/A rate. However, since there is some proton contamination in the out-FoV region of the PN<sup>38</sup> the Fin/Fout ratio saturates at a certain soft proton flux, while the Case B/A ratio keeps rising and appears to provide a more stable measurement of soft proton contamination in the PN, at least for our slew observations without bright targets. We investigate the properties of soft protons in section 3.4 in more detail.

Lastly, the Case C frames show a very similar trend to the Case A frames (Fig. 8 bottom right). The closed observations follow the Case A frames (Case C scatter 20%). Observations with the medium filter have Case C/A ratios that are also mostly constant, with some outliers, and their scatter is significantly larger (37%). However, apart from a few outliers, the Case C frames are mostly related to the Case A, and mainly particle induced.

### 3.3.2 Chandra HRC shield

The HRC shield count rates shows a very similar trend to the PN SWM Case A rates, where we clearly see the solar maxima with lower count rates around 2003 and 2014, and increased particle rates peaking in 2010 and 2020 (Fig. 9 purple data points in top panel). However, while the two datasets are highly consistent early on, the HRC shield rates appear to decline with time relative to the PN SWM (this effect is already corrected for in Fig. 9). This is expected due to the known increase in opacity in the scintillator and the loss of sensitivity over time of photomultiplier tubes (PMTs, e.g., 39). The PN SWM Case A frame rates can be used as a reference to correct the HRC shield rates. We implement a linear, time dependent function to match the HRC shield and PN SWM rates, while making sure to only include rates where both HRC shield and PN SWM data are available. For this scaling we use 24h time bins. Figure 9 (top panel) shows the PN SWM Case A measurements (blue) together with the scaled HRC shield count rates (purple). The correction terms account for a linear decrease in HRC shield sensitivity of 2.9% per year, and residuals are typically below 10% (see bottom panel in Fig. 9). The verification of the HRC shield data's consistency with PN SWM Case A rates highlights that two instruments on different satellites in slightly different orbits trace the same particle rate, which allows the application of conclusions from the high statistics HRC shield data to PN SWM data as well.

However, the residuals on long timescales (years) appear to follow the solar cycle (PN higher at solar maximum, lower panel of Fig. 9). The reason is likely a time variable spectrum of the GCRs (e.g., 40) that causes the distinct measurements in various instruments depending on the instruments energy sensitivity. Hardness ratios from Chandra ACIS in stowed position of the back-illuminated chips showed a similar variability<sup>41</sup>, which also leads to the conclusion of changes in



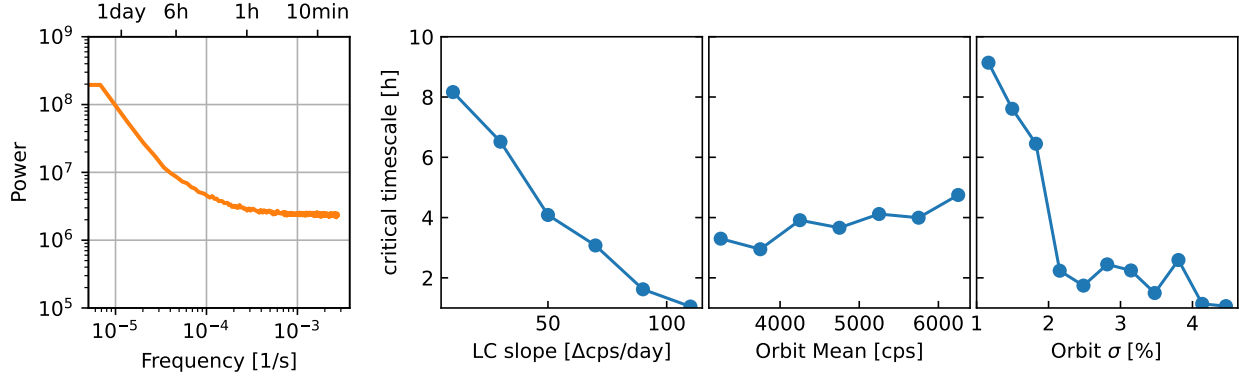


**Fig 10** Left: Power spectrum of the median HRC shield lightcurve, showing significant power in the particle background variability above 1 hour. The width of the dark orange bar represents the standard error, while the light orange shaded area shows the scatter of all power spectra. Three right panels: Dependence of the critical timescale (power increase by factor of 2) on orbital parameters (lightcurve slope, mean rate in each orbit, scatter in each orbit). A higher critical timescale represents a more quiescent particle background.

the CR properties. The HRC shield is most sensitive to particles with energies of tens of MeV, while the PN SWM Case A events are mostly induced by GeV protons. However, the scatter of these residuals also varies: From 2002 to 2005 the scatter was 5.7%, and during the next solar maximum, 2012 to 2016, it was 5.5%. In between the solar maxima, from 2006 to 2012, and from 2016 to 2022, the scatter was significantly lower (3.2% and 3.0%, respectively). We also reanalyzed these data with shorter time binning, instead of our default 24h, which results in higher values for the scatter. For example, for the 2006 to 2012 period, we get 3.6 (3.4, 3.2, 3.1, 2.9)% for 1, (6, 24, 48, 96) hour time bins, respectively. The trends are similar for the other intervals. We note that if the statistical uncertainty was the dominant source of scatter, we should expect much smaller values even for the 1h time binning, since the statistical uncertainty is typically 0.02% for HRC shield, and 1.2% for PN SWM. On the one hand, this clearly indicates that while the differences between HRC shield and PN SWM rates follow a normal distribution, they are systematic and time dependent. On the other hand, these residuals are more pronounced when comparing shorter time intervals, which emphasizes the importance to have a reliable background measurement close in time. It is possible that variations due to location (local magnetic field) can explain part of the residuals. A collection of simultaneous particle rate measurements in different orbits (other than XMM-Newton and Chandra) will help to quantify the orbital contribution to the residuals. I think that what you mean here is that can be variations due to location (i.e. the strength and connectivity of the local magnetic field), and therefore there will always be small amplitude differences between any two missions. Thus, we cannot rely on an external calibrator if we want to characterize the background to the degree required for studies of low surface brightness emission.

19 found a 6-day lag between the lightcurves of AMS and Chandra/XMM during the time period of 2016 and 2017. We searched for a similar time delay between lightcurves, making use of our superior time resolution. We re-extracted lightcurves on 30 min intervals, and after applying the previously calculated correction factor for the loss of PMT sensitivity, we utilize a timing analysis with a discrete correlation function. We find no time delays on any timescales of a less than 10 days. However, we find the peaks in the correlation function at 27 days time difference, and multiples 27 days. These are related to the (average) solar rotation timescale of sunspots.<sup>42-44</sup>

The wealth of information contained in the Chandra HRC shield dataset allows us to analyze a power spectrum of particle background variability. This utilizes the exceptional statistical power and extremely high time resolution with (almost) continuous observations for over 20 years. However, the elliptical orbit of Chandra passes through the Van Allen belts, which temporarily interrupts all science observations, including the operation of the HRC shield.<sup>45</sup> Therefore, the total orbital period of about 65 h permits continuous observations for only about 55 h. We derive a lightcurve of each Chandra orbit from the HRC shield rates, and quantify the orbital mean rate, its standard deviation, and the linear slope of the time dependence. We exclude the 3% of the most active orbits, where the scatter of the rates is at least 5%. For each orbital lightcurve we derive the power spectrum (PS) from the Fast Fourier Transformation (FFT), and stack all PS to derive the median PS. Figure 10 (left) shows the median power spectrum and its  $1\sigma$  scatter as the lightly shaded orange region, while the darker orange shade represents the standard error, which is relatively small due to the large number of orbits. The offset at the highest frequencies is due to the normalization of the FFT. The orbit-to-orbit scatter does not change with orbital properties, such as mean rate, slope or rate standard deviation. We can clearly see that there is more power on longer timescales, while on times below 1 h there is no significant power (variation consistent with the range of standard error). The longest timescale we can probe with our analysis is 2.3 days, the duration of the Chandra orbit outside the radiation belts. The shape of the power spectrum is well fit by a powerlaw plus constant, which allows us to define a critical timescale, at which the power reaches twice the constant baseline at high frequencies. The longer this critical timescale is, the less time variable is the particle background, and it can be assumed to be almost constant on timescales shorter than the critical timescale. For our default power spectrum, we derive a critical timescale of 3.9 h. In the three right panels of Figure 10 we test the dependence of this critical timescale on the orbital properties: For a strong linear trend meaning either a decreasing or increasing lightcurve, we find significantly shorter critical timescales (“slope”, which is measured as the absolute value), while, for the flattest lightcurves, critical timescales of up to 8 h are found. The mean rate in each orbit, mostly dependent on the solar cycle, is weakly correlated with the critical timescale. During solar minimum, fewer sunspots are present, but the particle background level is higher. However, fewer sunspots also imply a more stable background, and therefore longer critical timescales. Lastly, the scatter of the particle rate during an orbit is correlated very clearly with the critical timescale. Less than 2% scatter in the rate translates into critical timescales longer than 6 h, while the critical timescale is between 1 and 3 hours for orbits with greater scatter.

### 3.4 *Soft proton contamination*

We have analyzed the PN SWM lightcurves in section 3.3.1, where we concluded that the Case B/A frame ratio (frames with only valid events divided by only invalid event frames) can be used as a reliable soft proton contamination measure. As laid out there, this indicator can also be applied to all full frame (FF) observations in slew mode, since the Case A rate can be interpolated from Figure 8. In order to characterize the soft proton events further, we look at the fraction of single pattern events in these FF observations (with medium filter) and compare it with other datasets. Figure 11 shows the singles fractions versus the Case B/A estimator for the medium filter FF slew observation (blue). We categorize the soft proton contamination into 5 levels (numbers 1 through 5 in Fig. 11), and also show binned averages of the blue points in black. Observations free of soft protons flares have singles fractions around 65%, while the most extremely contaminated observations reach

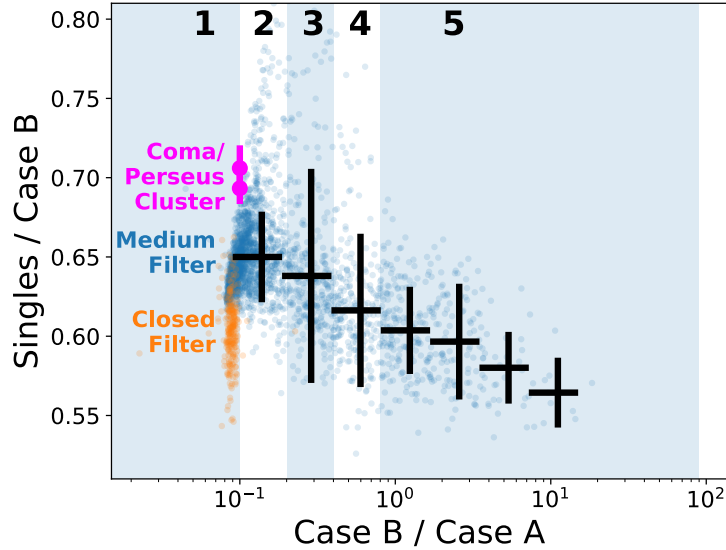


**Fig 11** Dependence of the single pattern fraction on the soft proton indicator, the Case B/A frame ratio. Blue points mark medium filter, full frame observations in slew mode (no science target), orange point show the distribution of closed filter observations, the two magenta point show the location of two very bright, extended X-ray sources. Black crosses are averages of the blue points. We define 5 levels of SP proton contamination, indicated by the labels 1 to 5.

55%. These averages clearly show that soft protons typically create fewer singles, meaning the charge is distributed over a larger number of pixels. The GCR particle background events (shown in orange) have a similar singles fraction to observations with strong soft proton contamination. A typical bright, diffuse or extended celestial X-ray source (in this case the bright clusters of galaxies Coma and Perseus) have higher singles fractions, around 70%. Since all of the slew observations are exposed to the diffuse X-ray foreground emission from the Galaxy, the Local Hot Bubble, and the Cosmic X-ray Background, but also to the particle background, it seems plausible that observations with few soft protons have singles fractions between the clusters and the closed filter observations.

After we have classified all the FF slew observations in the medium filter we can select a subset with high soft proton contamination and analyze the spectrum. We note that previous results<sup>46</sup> for the MOS cameras on XMM-Newton indicate a time variability of the spectrum of the soft proton induced X-ray background. While we see variations in the PN soft proton spectrum, we do not quantify this here. Instead, we concentrate on the average spectrum to be compared with simulations at a later stage. We focus exclusively on single events in the following, since they have the best statistics, and other patterns might have different spectra. In Fig. 12 we show the average spectrum of exposures around the 90<sup>th</sup> percentile of the Case B/A ratios after subtracting an average quiescent spectrum from it. The subtraction appears to be satisfactory since no fluorescent lines are present in the data (or absorption features from over-subtraction). The spectrum is well described by a powerlaw (index  $\alpha = 0.28$ ) with an exponential cutoff at around 9 keV. We note that this observed spectrum can motivate and verify detailed Geant4 simulations,<sup>47</sup> which will in turn allow a better modeling of the soft proton component in observations through tailored response matrices.

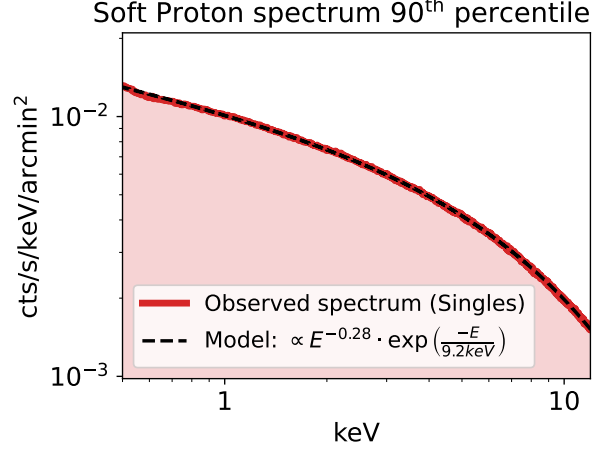


**Fig 12** Soft proton spectrum derived from observations within the 85th and 95th percentile of Case B/A ratios. The spectrum is “background subtracted”, meaning that an average spectrum with low Case B/A spectrum has been subtracted. The black dashed line shows a fit of a powerlaw function with exponential cutoff.

#### 4 Utilizing self anti-coincidence to reduce the particle background

Case C frames contain both, a particle track and an X-ray-like event. This provides additional information to reduce the particle background. Foremost, we can analyze the distance between a track and an X-ray event that occur in the same frame. Due to the short frame time of the SWM (5.6718 ms) there is a high chance that these events (valid and invalid in Case C) are correlated, meaning the particle also created the X-ray event (see also 18).

We know that all frames with invalid events,  $I$ , are Case A and C frames,  $I = A + C$ , while the valid event frames are Case B and C frames,  $X = B + C$ . If we assume for now, that the particle and X-ray events in Case C frames are random and not correlated, we can derive the expected number of C frames,

$$C = \frac{I \cdot X}{T} = \frac{(A + C) \cdot (B + C)}{T}, \quad (2)$$

where  $T$  is the total number of frames. The result can be compared to the actual number of Case C frames to provide insight into the absolute/integrated probability of correlated events in Case C frames. We note that a small number of frames can be misidentified, when a valid event is within 1 or 2 pixels of an invalid event in the same frame. We estimated the effect of this on the probability of correlated events in Case C frames to be less than 1 percent.

We can thus utilize the distance between particle tracks and X-ray events to derive a probability that the X-ray event was particle induced. For this we compare a random distribution of distances with the observed distance distribution, and normalize the result by the expected random number of Case C frames.

##### 4.1 Random distribution of distances

15 used an idealized random distribution for points on a disk of radius  $R$  to derive the probability function. However, assuming a disk instead of rectangular detector will introduce a small bias. In Section 3.1 we have derived the 2D distribution of events across the detector, which is nonuniform and should also be taken into account. We now derive empirically the distribution of random pair

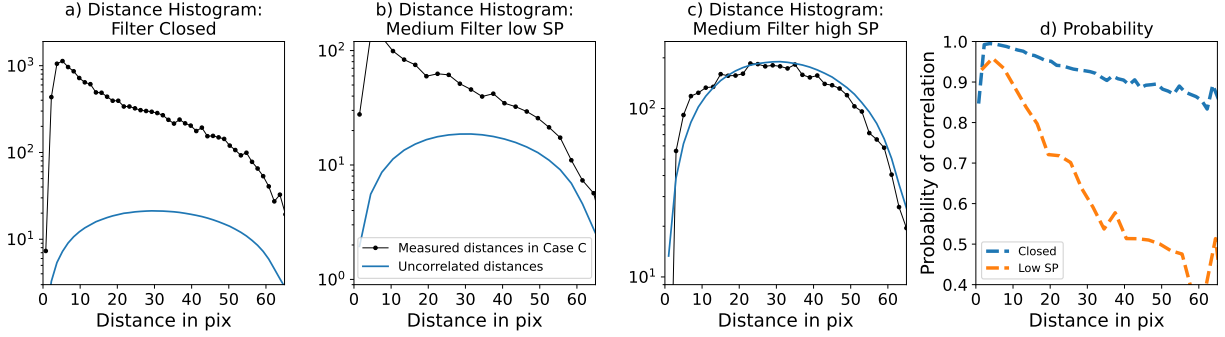


**Fig 13** Assessing the capabilities of self anti-coincidence (SAC). Panels a-c show the distribution of distances (black lines) between valid and invalid events in Case C frames, with only FWC observations in a), medium filter slew observations with low SP contamination in b), and, in c), for high SP contamination. The blue lines show the expected distribution for uncorrelated events. Panel d) shows the probability of an X-ray event at a given separation to the particle track, being induced by a particle (blue: closed filter observations, orange: medium filter with low SP). High soft proton contamination is not shown in d) as it is consistent with 0.

separations from the observed particle distribution on the detector (see Fig. 3 top left). We also take into account the distribution of valid events (as observed in Case B frames), which increases from the lowest to highest RAW Y column by  $\sim 30\%$ .

In order to compare the observed distribution of distances between X-ray and particle events in Case C frames, we use Eq. (2) to normalize our empirically determined random model. By comparing these distributions, the observed one and the random expectation, we can quantify at a given distance how likely an X-ray-like event is to be associated with a GCR. We show the two distributions (observed in black, random in blue) in Fig. 13, for (a) slew observations with the filter in the closed position, which means no sky X-rays are detected, for (b) slew observations with the medium filter and a low Case B/A ratio, meaning little soft proton contamination, and (c) medium filter observation with a very high soft proton (SP) contamination. We clearly see that shorter distances are generally more likely than larger distances, and that for FWC observations, the distribution of random coincidences underestimates the observed number of Case C events by at least an order of magnitude at all distances. We note that for distances of 0 or very few pixels we are unable to distinguish the X-ray event from the particle track. Therefore, extremely short distances ( $< 3$  pixels) are not reliable in Fig. 13. For the medium filter and low SP case, the shorter distances are highly over-represented with respect to the random expectation, while larger distances are almost in agreement. Finally, when there is intense soft proton contamination the agreement between the two curves is good, meaning almost none of the valid events in Case C frames are due to particle background events. These results are also reflected in panel (d) of Fig. 13, which shows the probability that an X-ray event at a given distance from the particle track is correlated with this track. Note that this is not a probability density function or probability distribution, and therefore the curves in Fig. 13 (d) do not add or integrated to 1. The FWC data are shown in blue, decreasing from about 100% at the shortest distances to about 88% at 64 pixel distance. This means, 96% of all FWC X-ray-like events in Case C frames are induced by a GCR. Uncertainties in finding the center for the particle track, and noise induced X-ray-like events cause the majority of the other 4% of events. The medium filter events in Fig. 13 (d, orange curve) reach close to 100% at the shortest distances, but decrease much more steeply to about 47% at 64 pixel, making about 78%

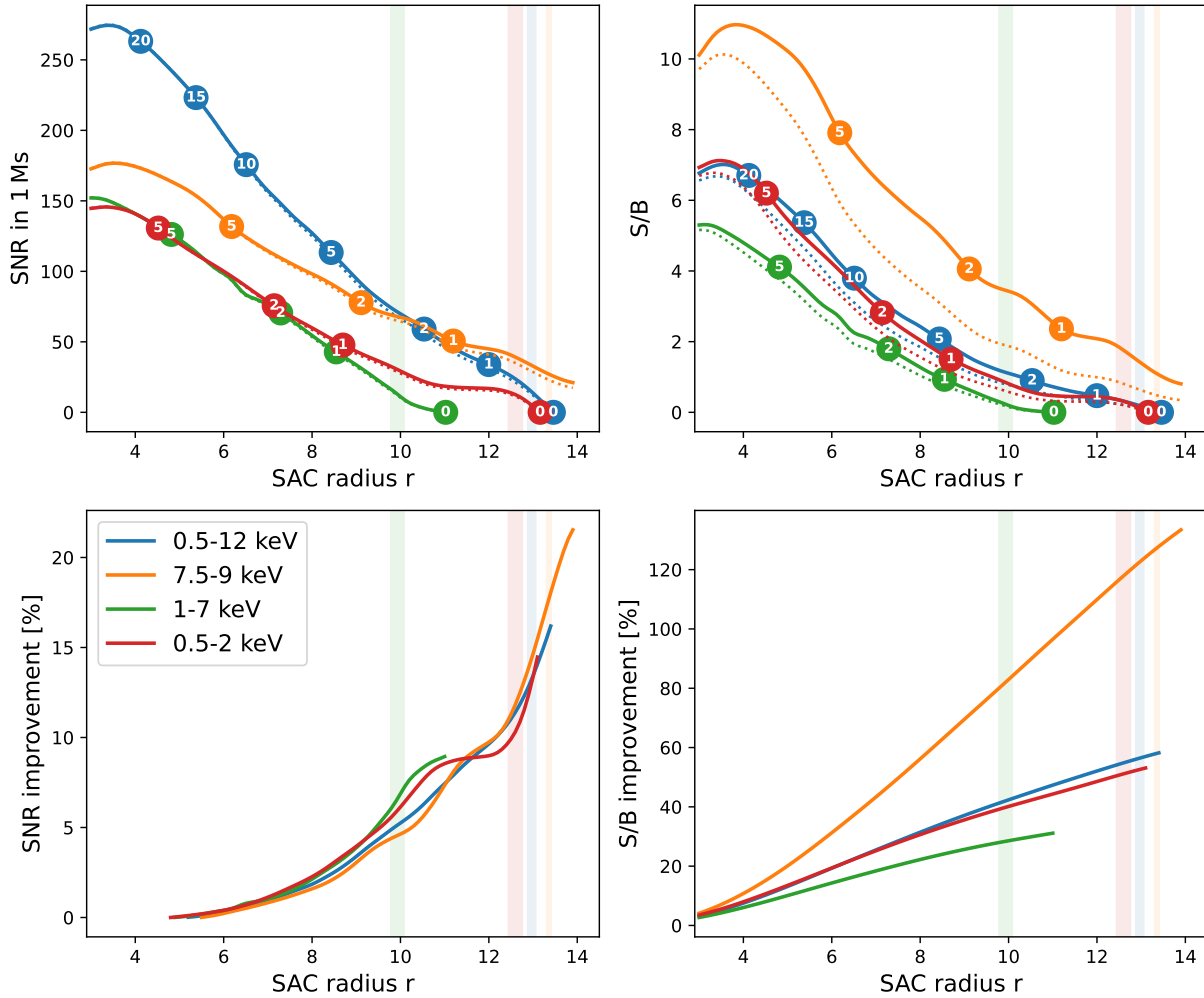


**Fig 14** Demonstration of the optimized self anti-coincidence (SAC) method. In all panels the x-axis is the optimized SAC radius for a given source brightness ( $r$  as a function of the source surface brightness). The top left (right) panel shows the signal-to-noise, SNR, (source to background ratio, S/B) as a function of the SAC exclusion radius, assuming a uniform source with the optimal brightness, and a 1 Ms exposure. The corresponding surface brightness values  $\bar{S}$  are indicated in the circles in units of  $\text{cts pix}^{-1} \text{Ms}^{-1}$ . The four different colors correspond to the energy bands of valid events listed in the legend below. Dotted lines refer to the SNR (S/B ratio) without SAC. The bottom panels show the improvement in % on the SNR and S/B. The shaded vertical bars indicate the median background level of blank sky observations (low SP case).

of all medium filter Case C X-ray events GCR induced. Note that we do not show the curve for the high soft proton observations, since it is essentially consistent with all events being unrelated to particle events. We also note that the statistics for very short distances ( $\leq 3$  pixel) are very poor and it becomes hard to clearly distinguish X-ray events from particle tracks.



## 4.2 Optimized self anti-coincidence

Here we consider how to optimize the signal-to-noise ratio for the Class C frames. We assume the signal-to-noise ratio to be

$$\text{SNR} = \frac{S}{\sqrt{S+B}}, \quad (3)$$

where  $S$  and  $B$  are the source and background counts. For a point source, the SNR is generally optimized by considering only events that lie close to the source position. However, the best strategy is different for extended sources. Our goal is to maximize the SNR when a circle of radius  $r$  is excluded around each particle event. We can determine  $S$  and  $B$  as functions of  $r$  simply by excluding events that lie too close to an invalid event, assuming that the source emission is uniform,

$$S(r) = \bar{S}(A_F - \pi r^2), \quad (4)$$

where  $\bar{S}$  is the average count per unit area, and  $A_F$  is the field of view area. For  $B(r)$ , we determine the total number of GCR induced X-ray events lying further than  $r$  from particle tracks. We empirically determine this by integrating the FWC distance distribution 13 from  $r$  to a large radius. The optimal  $r$  can be found by maximizing the SNR, i.e. by locating the zeroes of  $d\text{SNR}/dr$ , which yields

$$\bar{S} = -\frac{2B}{A_F - \pi r^2} - \frac{dB}{dr}. \quad (5)$$

This form relates surface brightness of the source to the optimal exclusion radius, in terms of the spatial distribution of the X-ray events induced by GCRs. It can be inverted to determine the optimal exclusion radius for a given source brightness. Since pixels are discrete, a GCR induced X-ray event cannot lie less than one pixel away from a track. Thus a meaningful  $B(r)$  can only be determined for  $r > 1$  pixel and meaningful values for  $\frac{dB}{dr}$  can only be determined for  $r \geq 5$  pixel. We find that  $\bar{S}$  given by equation (5) increases for small  $r$  to a maximum of  $\bar{S}_{\max}$ , before decreasing and, eventually, going negative for large  $r$ . Thus, this optimization is only feasible for surface brightnesses smaller than  $\bar{S}_{\max}$ . We note that  $\bar{S}_{\max}$  is proportional to the exposure time through the dependency on  $B$ .

The SNR must be an increasing function of  $r$  for values of  $r$  approaching the optimal exclusion radius from below. This requires  $A_F$  to be large compared to the core of the distribution of secondary particles. For the PN SWM we assume  $A_F = 64 \times 63$  pixel. If this condition is not met for  $r \rightarrow 0$ , the SNR cannot be improved by SAC. This assumes a uniform source distribution and ignores edge effects. For a uniform source distribution ( $\bar{S}$  in Eq. 4 is constant) we can easily derive the optimal SAC exclusion radius  $r$  based in Eq. 5 if we know  $B(r)$ . We can approximate  $B(r)$  based on the FWC distribution, shown in Fig. 13a), and also obtain the best achievable SNR through SAC using Eq. (5). We derive  $B(r)$  and  $\frac{dB}{dr}$  for various energy bands (see Fig. 15 for the 0.5 – 2 keV band as an example), and show the optimal SNR as a function of  $r$  in Fig. 14 (top left). For each energy band a radius  $r$  also corresponds to a surface brightness  $\bar{S}$ , and we indicated several values in the plot. Therefore, one can translate  $r$  into  $\bar{S}$ , and in turn derive a SNR without the use of SAC for comparison. These pre-SAC values are indicated as dashed lines, and only start deviating from the SAC improved SNRs for larger  $r$  and fainter sources. Note that the plot should not be interpreted as smaller radii resulting in a larger SNR, because each  $r$  is optimized for a specific source brightness  $\bar{S}$ .

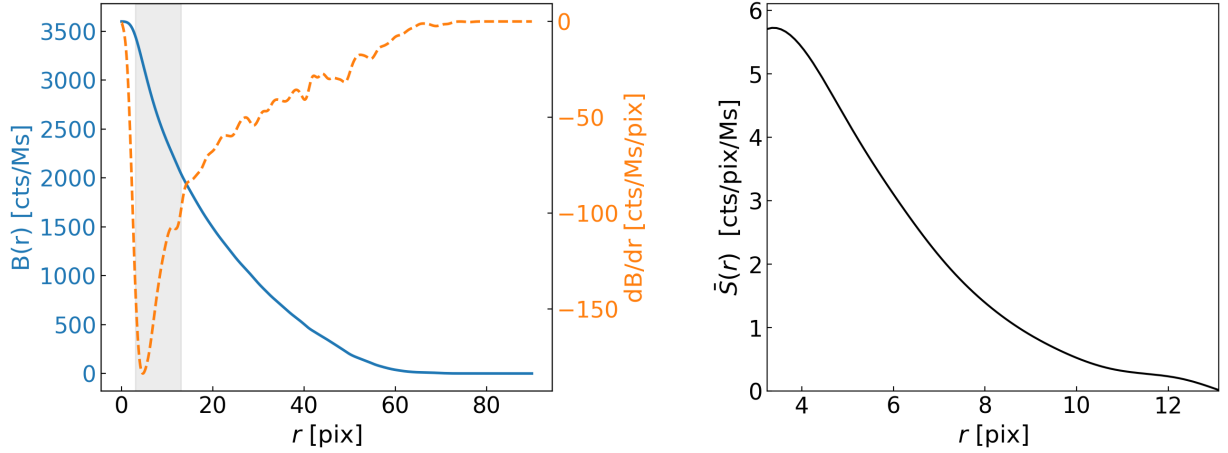


**Fig 15** Left: Dependence of  $B(r)$  (solid blue line, left axis), and  $\frac{dB}{dr}$  (dashed orange line, right axis) on the SAC radius  $r$ . Right:  $\bar{S}$  as a function of the SAC radius  $r$  following Eq. (5). Both panels show the 0.5 – 2 keV band results.

From a user perspective Eq. 5 is not intuitive, because the SAC radius  $r$  is the quantity to compute. Therefore, we provide a fitting function that parameterizes the observed trend,

$$r(\bar{S}) = A \left( \frac{\bar{S}}{s_0} \right)^{-\alpha} e^{-\frac{\bar{S}}{s_c}} \quad (6)$$

We find  $\alpha = 0.1$  and  $s_0 = 6.5 \text{ cts pix}^{-1} \text{ Ms}^{-1}$  to be constant for the 4 energy bands, while the amplitude  $A$  and cutoff brightness  $s_c$  vary: For  $A$  we find 11.2, 10.7, 7.7, and 8.3 pix for the 0.5 – 12, 7.5 – 9, 1 – 7, and 0.5 – 2 keV bands, respectively. For  $s_c$  the best fit values are 15.3, 8.2, 10.7, and 7.8  $\text{cts pix}^{-1} \text{ Ms}^{-1}$  for the same bands. The SRG/eROSITA All-Sky Survey (eRASS)<sup>48</sup> found an average surface brightness for the diffuse sky X-ray background in the 0.5 – 2 keV band of  $\sim 7 \times 10^{-12} \text{ erg s}^{-1} \text{ cm}^{-2} \text{ deg}^{-2}$ . For XMM PN this converts to a Case C count rate of roughly  $0.1 \text{ cts Ms}^{-1} \text{ pix}^{-1}$ . With Eq. (6) we can then compute the optimal SAC radius of  $r = 12 \text{ pix}$ .

In the top right panel of Fig. 14 we show the source to background ratio, S/B, which, unlike the SNR, is independent of the exposure time. The S/B is a good indicator of background systematics and when they become dominant over the results. The SNR, on the other hand, is a statistical measure of reliability of the results. While the curves look qualitatively similar to the SNR trends, the difference from the non-SAC values is much more pronounced. We quantify the improvement (Improvement defined as  $(\text{SNR}_{\text{SAC}} - \text{SNR}) \cdot \text{SNR}^{-1}$ , and for S/B accordingly) of both, the SNR and S/B, in the bottom panels of Fig. 14. For fainter sources and therefore larger  $r$  we find a stronger improvement of both, the SNR and S/B. While the SNR improvement is overall less significant ( $< 25\%$ ), the S/B improvement can reach 50% and more. However, the S/B flattens at larger radii, while the SNR is increasing drastically with radius. We note that the optimal  $r$  shown in Fig. 14 is derived for maximizing the SNR, not the S/B. All four panels of Fig. 14 also show the median blank sky background (as vertical bars), as estimated from the medium filter slew observations with low SP contamination.

We verified the assumption of average slew data representing the blank sky by looking at the Case C frames of a PN SWM pointed observation of NGC 7314 (obsid 0725200101). We find that, after removing a region of 28 arcsec radius around the bright source, the average surface

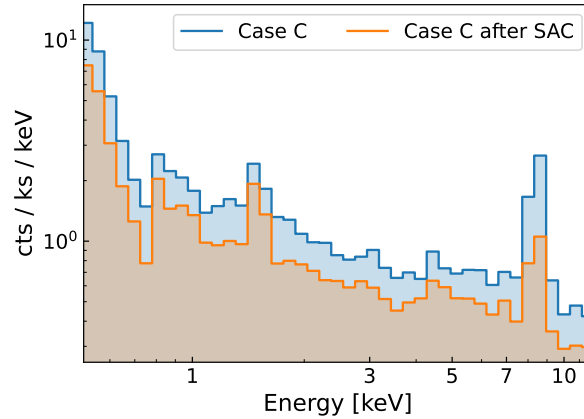


**Fig 16** Case C valid event spectrum of blank sky/slew observations before and after applying the optimized SAC method. The SNR improves as expected.

brightness (after subtracting the expected Case C background events based on FWC observations) is  $0.48 \text{ cts Ms}^{-1} \text{ pix}^{-1}$  in the (0.5 – 12) keV band, which is in full agreement with the slew rates (see Fig. 14). The blank sky background definitely fulfills the source requirement of uniformity across the detector, and is at the faint end of all tested surface brightness values. We also tested filtering by event pattern, but found only a small improvement for singles exclusively. In Figure 16 we illustrate the improvement of optimized SAC for the Case C spectrum of the 230 ks medium filter slew observations. The unfiltered spectrum (blue) consists of the NXB and the average sky foreground and background emission. After applying the optimized SAC by filtering out X-ray like events based on the distance to the particle track, we find that especially the line-free energies from 1 to 7 keV (without the Al line) has been greatly reduced (see orange curve in Fig. 16). From a total of 3305 counts, 2053 are left after SAC. Based on FWC observation, we estimate a total of 2850 NXB counts, and 1584 NXB counts if SAC is applied to these observations in the same way. While the original SNR of 7.9 is expected to increase to about 9.1 (based on Fig. 14) we find that SAC indeed improves the SNR to 10.3. The source/background ratio improves from 0.16 to 0.30, where the expectation was 0.26. This demonstrates that our optimization method for SAC is viable, and can improve the signal of faint diffuse sources, in this case the sky X-ray background.

While this experiment shows that the SNR can only be improved marginally by SAC for SWM observations, the obvious next step would be a larger detector area. Each of the 4 quadrants of the large detector of the Athena/WFI will have 64 times the area of the PN SWM region.

## 5 Summary

Many characteristics of the particle induced background in X-ray observations, such as its variability, are either unknown, or have large uncertainties, which limits our ability to make optimal use of the X-ray data. By utilizing the PN SWM data we have significantly improved our knowledge of the NXB. The combination of a short frame time of 5.67 ms and disabled onboard MIP rejection allowed the detected events to be classified into valid (X-ray like) and invalid (particle-like) events, based on their energy and pattern signatures. This enabled us to study the statistical properties and correlations of the NXB and particle events:

- From 626 slew observations in SWM and 519 in closed filter mode we found a distribution of particle tracks that is consistent with expectations: The spatial distribution of the tracks reflects the readout pattern, while the orientation is more uniform. However, we find that the length distribution of these particle track “islands” is not always consistent with a simple box detector model, where charge is equally distributed along the path through the 3D detector volume. We exclude edge effects by only selecting islands in the central part of the detector, and find that there is still an excess of shorter tracks with respect to our model, while the distribution of longer tracks is roughly consistent. The cause of these shorter particle tracks is unclear.
- The spectrum of valid events features several fluorescent X-ray lines, most prominently from Al, Cu and Zn. Interestingly, in frames that also contain invalid events the line flux is much higher, and the line energy of Cu and Zn is shifted to slightly lower energies, while all other fluorescent lines remain unchanged. This shift is likely due to the enhanced detection of Cu/Zn during readout, while the hole in the electronics board over the SWM aperture makes it more difficult to produce these lines during exposure to the sky.
- The variability with time of the number of frames with particle tracks is well-correlated with the solar cycle. The rate of valid events shows no additional variability in FWC observations, while the rate of valid events varies by over two orders of magnitude during slew observations with the filter open. This can be attributed to soft protons.
- Comparing the numbers of valid and invalid events allowed observations that are highly contaminated by soft protons to be identified among full frame slew observations (not SWM). Using them, a model was derived for the average soft proton spectrum, consisting of a shallow powerlaw (index  $-0.28$ ) with an exponential drop at around 9 to 10 keV. Soft protons produce a low fraction of single events compared to normal celestial X-rays.
- A comparison between the detailed lightcurve of particle events in SWM and statistically superior Chandra HRC shield rates shows very good agreement. However, we detect residuals on various time scales, which require more investigation, as they might be related to changes in the GCR spectrum. No temporal offset between the detectors on the two satellites can be identified. A power spectrum analysis of the Chandra HRC shield data allows the definition of a critical timescale on the order of hours, within which the background shows negligible variability.
- Frames with both particle events and X-ray like events have a special importance, since there is a high chance of the X-ray event being particle induced through secondaries. We quantify the likelihood of association between X-ray and particle events as a function of their separation. As expected, X-ray events in FWC observations are almost 100% particle induced, while medium filter observations with low soft proton contamination have a high chance of correlation only for very small separations. A self anti-coincidence method of removing events based on the particle separation can be improved by maximizing the SNR in distinct energy bands. While for very faint sources the improvement can be substantial, the impact is greatly limited by the small aperture of the SWM.

## Disclosures

The authors declare that there are no financial interests, commercial affiliations, or other potential conflicts of interest that could have influenced the objectivity of this research or the writing of this paper.

## Code and Data Availability

The XMM-Newton data presented in this article are publicly available through the ESAC Science Data Centre <https://www.cosmos.esa.int/web/xmm-newton/xsa>. Chandra HRC Anti-Coincidence shield data are available upon request.

## Acknowledgments

We gratefully acknowledge support from NASA grant NNX17AB07G, administered by The Pennsylvania State University. This work was done as part of the Athena WFI Background Working Group, a consortium including MPE, INAF/IASF-Milano, IAAT, Open University, MIT, SAO, and Stanford. We would like to thank the entire Working Group for valuable discussions that contributed greatly to this paper.

This research has made use of data obtained from the Chandra Data Archive provided by the Chandra X-ray Center (CXC), and the archival data from XMM-Newton, an ESA science mission with instruments and contributions directly funded by ESA Member States and NASA. This research utilized the following software libraries for data analysis and presentation: XMM-Newton SAS,<sup>22</sup> Astropy<sup>49,50</sup> a community-developed core Python package for Astronomy; Matplotlib<sup>51</sup> a Python library for publication quality graphics; NumPy<sup>52</sup> a structure for efficient numerical computation; SciPy<sup>53</sup> Open Source Scientific Tools for Python; and the GNU Scientific Library.

## References

- 1 K. Nandra, D. Barret, X. Barcons, *et al.*, “The hot and energetic universe: A white paper presenting the science theme motivating the athena+ mission,” *arXiv [astro-ph.HE]* 1306.2307 (2013).
- 2 A. Rau, N. Meidinger, K. Nandra, *et al.*, “The hot and energetic universe: The wide field imager (WFI) for athena+,” *arXiv [astro-ph.IM]* 1308.6785 (2013).
- 3 N. Meidinger, M. Barbera, V. Emberger, *et al.*, “The wide field imager instrument for athena,” in *UV, X-Ray, and Gamma-Ray Space Instrumentation for Astronomy XX*, **10397**, 245–256, SPIE (2017).
- 4 A. Leccardi and S. Molendi, “Radial temperature profiles for a large sample of galaxy clusters observed with XMM-Newton,” *Astron. Astrophys.* **486**, 359–373 (2008).
- 5 S. Ettori, G. W. Pratt, J. de Plaa, *et al.*, “The hot and energetic universe: The astrophysics of galaxy groups and clusters,” *arXiv [astro-ph.HE]* 1306.2322 (2013).
- 6 A. Georgakakis, F. Carrera, G. Lanzuisi, *et al.*, “The hot and energetic universe: Understanding the build-up of supermassive black holes and galaxies at the heyday of the universe,” *arXiv [astro-ph.HE]* 1306.2328 (2013).
- 7 H. V. Neher and H. R. Anderson, “Cosmic rays at balloon altitudes and the solar cycle,” *J. Geophys. Res.* **67**, 1309–1315 (1962).

- 8 I. Ferreira, M. Ayre, M. Bavdaz, *et al.*, “Design of the charged particle diverter for the ATHENA mission,” in *Space Telescopes and Instrumentation 2018: Ultraviolet to Gamma Ray*, J.-W. A. den Herder, K. Nakazawa, and S. Nikzad, Eds., **10699**, 106994A, SPIE (2018).
- 9 V. Fioretti, A. Bulgarelli, S. Molendi, *et al.*, “Magnetic shielding of soft protons in future X-ray telescopes: The case of the ATHENA wide field imager,” *Astrophys. J.* **867**, 9 (2018).
- 10 J.-P. Breuer, G. Galgóczi, V. Fioretti, *et al.*, “Athena charged particle diverter simulations: effects of micro-roughness on proton scattering using Geant4,” in *Space Telescopes and Instrumentation 2022: Ultraviolet to Gamma Ray*, J.-W. A. den Herder, K. Nakazawa, and S. Nikzad, Eds., **12181**, 1040–1051, SPIE (2022).
- 11 G. Galgóczi, J.-P. Breuer, V. Fioretti, *et al.*, “Geant4 simulation of the residual background in the ATHENA wide field imager from protons deflected by the charged particle diverter,” in *Space Telescopes and Instrumentation 2022: Ultraviolet to Gamma Ray*, J.-W. A. den Herder, K. Nakazawa, and S. Nikzad, Eds., **12181**, 1015–1023, SPIE (2022).
- 12 H. Katayama, I. Takahashi, Y. Ikebe, *et al.*, “Properties of the background of EPIC-pn on-board XMM-newton,” *Astron. Astrophys.* **414**, 767–776 (2004).
- 13 K. Dennerl, B. Aschenbach, U. G. Briel, *et al.*, “Improving XMM-newton EPIC pn data at low energies: method and application to the vela SNR,” *UV and Gamma* (2004).
- 14 C. E. Grant, E. D. Miller, M. W. Bautz, *et al.*, “Reducing the ATHENA WFI background with the science products module: lessons from chandra ACIS,” in *Space Telescopes and Instrumentation 2018: Ultraviolet to Gamma Ray*, **10699**, 106994H, International Society for Optics and Photonics (2018).
- 15 E. Bulbul, R. Kraft, P. Nulsen, *et al.*, “Characterization of the particle-induced background of XMM-newton EPIC-pn: Short- and long-term variability,” *ApJ* **891**, 13 (2020).
- 16 C. E. Grant, E. D. Miller, M. W. Bautz, *et al.*, “Reducing the athena WFI charged particle background: results from Geant4 simulations,” in *Space Telescopes and Instrumentation 2020: Ultraviolet to Gamma Ray*, **11444**, 1144442, International Society for Optics and Photonics (2020).
- 17 D. Wilkins, S. Allen, E. D. Miller, *et al.*, “Identifying charged particle background events in x-ray imaging detectors with novel machine learning algorithms,” in *Space Telescopes and Instrumentation 2020: Ultraviolet to Gamma Ray*, J.-W. A. den Herder, K. Nakazawa, and S. Nikzad, Eds., SPIE (2020).
- 18 E. D. Miller, C. E. Grant, M. W. Bautz, *et al.*, “Mitigating the effects of particle background on the athena wide field imager,” *JATIS* **8**, 018001 (2022).
- 19 A. Sarkar, C. E. Grant, E. D. Miller, *et al.*, “Advancing precision particle background estimation for future X-ray missions: Correlated variability between the alpha magnetic spectrometer and chandra/XMM-newton,” *Astrophys. J.* **970**, 22 (2024).
- 20 U. G. Briel, “EPIC-pn camera onboard XMM-newton: performance and scientific results,” *X-Ray and Gamma-Ray Telescopes and Instruments for Astronomy* (2003).
- 21 B. M. Walsh, K. D. Kuntz, M. R. Collier, *et al.*, “Energetic particle impact on X-ray imaging with XMM-newton,” *Space Weather* **12**, 387–394 (2014).
- 22 C. Gabriel, M. Denby, D. J. Fyfe, *et al.*, “The XMM-newton SAS-distributed development and maintenance of a large science analysis system: a critical analysis,” *Astronomical Data* (2004).



- 23 S. S. Murray, G. K. Austin, J. H. Chappell, *et al.*, “In-flight performance of the chandra high-resolution camera,” in *X-Ray Optics, Instruments, and Missions III*, **4012**, 68–80, SPIE (2000).
- 24 S. L. O’Dell, T. L. Aldcroft, B. A. Bissell, *et al.*, “Managing radiation degradation of CCDs on the chandra X-ray observatory II,” in *UV, X-Ray, and Gamma-Ray Space Instrumentation for Astronomy XIV*, **5898**, 212–223, SPIE (2005).
- 25 T. Eraerds, V. Antonelli, C. Davis, *et al.*, “Enhanced simulations on the athena/wide field imager instrumental background,” *J. Astron. Telesc. Instrum. Syst.* **7**, 034001 (2021).
- 26 R. Jain, R. Kasturi, and B. G. Schunck, *Machine Vision*, McGraw-Hill (1995).
- 27 M. Kuster, S. Benlloch, E. Kendziorra, *et al.*, “Time resolution capability of the XMM EPIC pn-CCD in different readout modes,” in *EUV, X-Ray, and Gamma-Ray Instrumentation for Astronomy X*, O. H. W. Siegmund and K. A. Flanagan, Eds., **3765**, 673–682, SPIE (1999).
- 28 D. H. Lumb, R. S. Warwick, M. Page, *et al.*, “X-ray background measurements with XMM-newton EPIC,” *Astron. Astrophys.* **389**, 93–105 (2002).
- 29 A. M. Read and T. J. Ponman, “The XMM-newton EPIC background: Production of background maps and event files,” *Astron. Astrophys.* **409**, 395–410 (2003).
- 30 V. Bender, G. De Canio, M. J. Freyberg, *et al.*, “Analysis of minimum ionising particles and soft protons using XMM-newton EPIC pn-CCD as a particle detector,” *Astron. Astrophys. Suppl. Ser.* **670**, A78 (2023).
- 31 J. A. Carter and A. M. Read, “The XMM-newton EPIC background and the production of background blank sky event files,” *Astron. Astrophys. Suppl. Ser.* **464**(3), 1155–1166 (2007).
- 32 M. J. Freyberg, U. G. Briel, K. Dennerl, *et al.*, “EPIC pn-CCD detector aboard XMM-newton: status of the background calibration,” in *X-Ray and Gamma-Ray Instrumentation for Astronomy XIII*, **5165**, 112–122, SPIE (2004).
- 33 L. Strüder, J. Enghauser, R. Hartmann, *et al.*, “pnCCDs on XMM-Newton—42 months in orbit,” *Nucl. Instrum. Methods Phys. Res. A* **512**, 386–400 (2003).
- 34 L. J. Gleeson and W. I. Axford, “Solar modulation of galactic cosmic rays,” *Astrophys. J.* **154**, 1011 (1968).
- 35 B. Aschenbach, “Grazing incidence reflection and scattering of MeV protons,” in *Optics for EUV, X-Ray, and Gamma-Ray Astronomy III*, S. L. O’Dell and G. Pareschi, Eds., **6688**, 157–163, SPIE (2007).
- 36 V. Fioretti, on behalf of the AREMBES collaboration, T. Mineo, *et al.*, “Geant4 simulations of soft proton scattering in X-ray optics: A tentative validation using laboratory measurements,” *Exp. Astron.* **44**, 413–435 (2017).
- 37 A. De Luca and S. Molendi, “The 2–8 keV cosmic X-ray background spectrum as observed with XMM-newton,” *Astron. Astrophys. Suppl. Ser.* **419**(3), 837–848 (2004).
- 38 M. Marelli, S. Molendi, M. Rossetti, *et al.*, “Analysis of the unconcentrated background of the EPIC pn camera on board XMM-newton,” *ApJ* **908**, 37 (2021).
- 39 L. Hum, P.-S. Shaw, Z. Li, *et al.*, “Ultraviolet degradation study of photomultiplier tubes at SURF III,” in *Chemical, Biological, Radiological, Nuclear, and Explosives (CBRNE) Sensing X*, A. W. Fountain, III and P. J. Gardner, Eds., **7304**, 260–267, SPIE (2009).
- 40 N. Yamashita, N. Hasebe, T. Miyachi, *et al.*, “Complexities of gamma-ray line intensities from the lunar surface,” *Earth Planets Space* **60**, 313–319 (2008).

- 41 H. Suzuki, P. P. Plucinsky, T. J. Gaetz, *et al.*, “Spatial and temporal variations of the chandra ACIS particle-induced background and development of a spectral-model generation tool,” *Astron. Astrophys.* **655**, A116 (2021).
- 42 R. C. Willson and H. S. Hudson, “Solar luminosity variations in solar cycle 21,” *Nature* **332**, 810–812 (1988).
- 43 J. G. Beck, “A comparison of differential rotation measurements – (invited review),” *Sol. Phys.* **191**, 47–70 (2000).
- 44 Y. Reuveni and C. Price, “A new approach for monitoring the 27-day solar rotation using VLF radio signals on the earth’s surface: VLF AND THE 27-DAY SOLAR ROTATION,” *J. Geophys. Res.* **114** (2009).
- 45 S. N. Virani, R. Mueller-Mellin, P. P. Plucinsky, *et al.*, “The chandra X-ray observatory’s radiation environment and the AP-8/AE-8 model,” *arXiv [astro-ph] 0004177* (2000).
- 46 K. D. Kuntz and S. L. Snowden, “The EPIC-MOS particle-induced background spectra,” *Astron. Astrophys. Suppl. Ser.* **478**(2), 575–596 (2008).
- 47 V. Fioretti, T. Mineo, R. Amato, *et al.*, “Design and characterization of a prototype proton response matrix for the XMM-newton mission,” in *Optics for EUV, X-Ray, and Gamma-Ray Astronomy X*, **11822**, 232–242, SPIE (2021).
- 48 M. C. H. Yeung, M. J. Freyberg, G. Ponti, *et al.*, “SRG/eROSITA X-ray shadowing study of giant molecular clouds,” *arXiv [astro-ph.GA]*, A3 (2023).
- 49 The Astropy Collaboration, T. P. Robitaille, E. J. Tollerud, *et al.*, “Astropy: A community python package for astronomy,” *Astron. Astrophys. Suppl. Ser.* **558**, A33 (2013).
- 50 The Astropy Collaboration, A. M. Price-Whelan, B. M. Sipőcz, *et al.*, “The astropy project: Building an open-science project and status of the v2.0 core package,” *Astron. J.* **156**(3), 123 (2018).
- 51 J. D. Hunter, “Matplotlib: A 2D graphics environment,” *Comput. Sci. Eng.* **9**, 90–95 (2007).
- 52 S. van der Walt, S. C. Colbert, and G. Varoquaux, “The NumPy array: A structure for efficient numerical computation,” *Comput. Sci. Eng.* **13**, 22–30 (2011).
- 53 E. Jones, T. Oliphant, and P. Peterson, “SciPy: Open source scientific tools for python,” (2001).

**Gerrit Schellenberger** is an Astrophysicist at the Center for Astrophysics | Harvard & Smithsonian. He received his BS and MS degrees in physics and astrophysics from Bonn University, Germany, in 2010 and 2012, respectively, and his PhD degree in Astronomy and Astrophysics from Bonn University in 2016. He is the author of more than 60 journal papers and is a Chandra HRC Project Scientist. His current research interests include multiwavelength observations of clusters and groups of galaxies, and systematic uncertainties in X-ray observations.

## Appendix A: List of Small Window Mode observations

Table 1 lists all 626 slew observation in Small Window Mode that were used for this work. Column (2) is the filter used on PN, which is either Medium (Med), Closed (FWC), or Closed with calibration source (Cal). Column (4) gives the total number of Small Window Mode frames, and Column (5) the fraction of Case A frames in per mille.

Table 1: XMM-Newton PN observations in Small Window Mode during slews.

OBSID	Filter	Date	Total	Case A	OBSID	Filter	Date	Total	Case A
(1)	(2)	Y/M/D	Frames	%	(1)	(2)	Y/M/D	Frames	%
(1)	(2)	(3)	(4)	(5)	(1)	(2)	(3)	(4)	(5)
903800005	Med	2002/01/06	523468	6.4	904250003	Med	2002/04/05	523474	6.3
904290002	Med	2002/04/13	523496	6.3	904420003	Med	2002/05/09	341345	6.4
904500003	Med	2002/05/25	1069367	6.7	904560004	Med	2002/06/06	329364	6.8
904590002	Med	2002/06/11	306525	6.5	904610002	Med	2002/06/15	566369	6.7
904870002	Med	2002/08/06	262045	5.8	905090005	Med	2002/09/20	496700	6.4
905100004	Med	2002/09/22	574413	6.4	905130005	Med	2002/09/28	507731	6.4
905310005	Med	2002/11/02	237862	6.3	905690004	Med	2003/01/17	865059	7.0
905720003	Med	2003/01/23	475199	6.6	905720004	Med	2003/01/23	519871	6.3
905730003	Med	2003/01/24	310481	6.4	905730006	Med	2003/01/25	580922	6.3
905750006	Med	2003/01/30	776980	7.0	905860004	Med	2003/02/20	498185	6.3
905930004	Med	2003/03/06	474724	7.0	905940002	Med	2003/03/08	334664	6.7
905950004	Med	2003/03/10	498657	6.6	906330005	Med	2003/05/25	495015	7.0
906430004	Med	2003/06/14	551321	6.7	906680004	Med	2003/08/03	567247	6.5
906710004	Med	2003/08/09	493926	6.5	906830004	Med	2003/09/02	282502	6.4
906900004	Med	2003/09/15	655746	6.8	907070004	Med	2003/10/19	250470	7.0
907240008	Med	2003/11/23	526419	5.5	907350004	Med	2003/12/14	268620	6.1
907580004	Med	2004/01/29	280126	6.6	907690004	Med	2004/02/20	1038827	7.2
907700007	Med	2004/02/22	382938	7.1	907770004	Med	2004/03/07	208573	7.2
907780005	Med	2004/03/09	237174	7.2	907800008	Med	2004/03/13	458472	8.4
908310003	Med	2004/06/22	682729	7.9	908320004	Med	2004/06/25	426727	8.1
908370002	Med	2004/07/05	897313	8.2	908440005	Med	2004/07/19	217153	8.1
908490005	Med	2004/07/29	519693	7.8	908540004	Med	2004/08/08	480407	7.9
908770004	Med	2004/09/23	499699	7.8	908820003	Med	2004/10/03	494696	8.8
908840004	Med	2004/10/06	881434	8.8	908840005	Med	2004/10/07	562665	8.7
908880003	Med	2004/10/14	882462	8.7	908930002	Med	2004/10/24	277918	8.9
908940002	Med	2004/10/26	477624	8.8	908960003	Med	2004/10/30	571206	8.9
909040003	Med	2004/11/15	230488	7.6	909080002	Med	2004/11/23	257771	8.9
909120002	Med	2004/12/01	1078289	8.8	909210003	Cal	2004/12/19	683028	8.5
909220003	Cal	2004/12/21	721744	8.6	909300002	Cal	2005/01/06	637169	7.6
909390004	Cal	2005/01/24	244076	7.9	909410002	Cal	2005/01/28	371449	8.2
909410004	Cal	2005/01/28	460583	8.3	909520004	Cal	2005/02/19	492603	7.8
909590002	Med	2005/03/04	961654	8.3	909590006	Med	2005/03/05	281505	8.9
909600004	Med	2005/03/07	344912	8.6	909680005	Med	2005/03/23	330852	7.7
909720003	Med	2005/03/31	204845	8.3	909790002	FWC	2005/04/13	971854	8.6
909930005	Med	2005/05/12	662686	9.5	910040003	Med	2005/06/03	563154	8.7
910140003	Med	2005/06/22	432545	8.9	910160003	Med	2005/06/26	886969	8.7
910170002	Med	2005/06/28	167511	8.4	910200010	Med	2005/07/05	313362	9.0
910270003	Med	2005/07/19	551682	7.8	910420005	Med	2005/08/17	325331	8.3
910470006	Med	2005/08/28	1010313	8.5	910610004	Med	2005/09/24	342233	7.8
910630005	Med	2005/09/29	178251	8.3	910650002	Med	2005/10/02	526588	8.4
910730002	Med	2005/10/19	715510	9.1	910820004	Med	2005/11/05	160843	8.9
910950002	Med	2005/12/01	1000085	9.3	911290003	Med	2006/02/07	374145	10.0
911420002	Med	2006/03/05	203674	10.3	911490002	Med	2006/03/19	231332	10.4
911530002	Med	2006/03/27	311262	10.2	911580002	Med	2006/04/06	477591	10.3
911650004	Med	2006/04/20	1172741	10.5	911680003	Med	2006/04/26	937027	10.6
911930003	Med	2006/06/14	953546	10.7	912020004	Med	2006/07/03	302797	11.0
912230002	Med	2006/08/13	559123	10.8	912240002	Med	2006/08/15	432807	10.8
912250003	Med	2006/08/17	221949	10.7	912270002	Med	2006/08/21	522650	10.1

## Continuation of Table 1

(1)	(2)	(3)	(4)	(5)	(1)	(2)	(3)	(4)	(5)
9124600002	Med	2006/09/28	266130	10.8	9124700002	Med	2006/09/30	761052	10.6
9124700003	Med	2006/09/30	1176258	10.6	9125100003	Med	2006/10/08	620406	10.9
9125400002	Med	2006/10/14	252815	10.8	9125700003	Med	2006/10/20	825923	11.1
9125900002	Med	2006/10/24	1116477	11.0	9126300004	Med	2006/11/01	186605	11.1
9126300005	Med	2006/11/02	211586	11.3	9126400002	Med	2006/11/03	298936	11.1
9126500002	Med	2006/11/05	369890	11.2	9126600002	Med	2006/11/08	680432	10.9
9130000002	Med	2007/01/13	1141952	11.2	9131100004	Med	2007/02/05	744510	11.1
9131300004	Med	2007/02/09	1122224	10.9	9132900004	Med	2007/03/13	722415	9.9
9133000003	Med	2007/03/15	177891	11.0	9133200004	Med	2007/03/19	361499	11.5
9133300003	Med	2007/03/21	204769	11.4	9134300002	Med	2007/04/10	411539	11.6
9134700002	Med	2007/04/18	693924	11.6	9134900002	Med	2007/04/22	414767	11.7
9136000003	FWC	2007/05/13	690115	12.0	9136100002	FWC	2007/05/16	418639	12.0
9136200004	FWC	2007/05/18	1132077	11.9	9136500003	FWC	2007/05/23	717519	11.5
9137500005	FWC	2007/06/12	995629	11.9	9138800003	FWC	2007/07/08	395751	12.2
9138900004	FWC	2007/07/11	778930	11.9	9139200003	FWC	2007/07/17	504354	11.9
9139400002	FWC	2007/07/20	201915	11.8	9139500004	FWC	2007/07/23	759509	11.9
9139700002	FWC	2007/07/26	383898	12.3	9140100004	FWC	2007/08/03	241881	11.9
9141000003	FWC	2007/08/21	719021	12.1	9142800004	FWC	2007/09/26	1005948	12.1
9143300002	FWC	2007/10/06	654472	12.2	9144300004	FWC	2007/10/26	1087657	12.0
9144500003	FWC	2007/10/30	522940	12.0	9144700003	FWC	2007/11/03	175325	11.7
9144900005	FWC	2007/11/08	234024	13.0	9145700003	FWC	2007/11/23	917227	11.7
9146300006	FWC	2007/12/05	587071	12.4	9147500002	FWC	2007/12/28	330882	12.6
9147900002	FWC	2008/01/05	327374	12.5	9148000004	FWC	2008/01/08	225990	11.7
9148400003	FWC	2008/01/16	440017	11.9	9149500002	FWC	2008/02/07	838018	12.1
9151000002	FWC	2008/03/08	1175237	11.8	9151000003	FWC	2008/03/08	632727	12.1
9151300002	FWC	2008/03/14	922996	11.7	9151600004	FWC	2008/03/20	349685	11.9
9151700002	FWC	2008/03/22	168322	12.4	9152300002	FWC	2008/04/02	377645	11.9
9152400002	FWC	2008/04/04	585622	11.9	9152700003	FWC	2008/04/11	667737	11.8
9152900002	FWC	2008/04/14	624744	11.9	9153000003	FWC	2008/04/16	735807	11.9
9153100004	FWC	2008/04/19	1007745	12.0	9153200003	FWC	2008/04/21	936524	12.1
9153300002	FWC	2008/04/22	827870	12.1	9153400002	FWC	2008/04/25	652006	11.8
9153400004	FWC	2008/04/25	868326	11.7	9153600002	FWC	2008/04/28	964646	12.1
9153600003	FWC	2008/04/29	1090252	12.1	9153900002	FWC	2008/05/05	184263	11.9
9154200004	FWC	2008/05/11	1103387	12.1	9154300003	FWC	2008/05/13	510530	12.0
9154400005	FWC	2008/05/15	536232	12.1	9154600005	FWC	2008/05/19	773230	12.2
9156800003	FWC	2008/07/02	1027722	12.3	9158100002	FWC	2008/07/28	822192	12.2
9158900004	FWC	2008/08/12	589018	12.2	9160000002	FWC	2008/09/03	578524	12.9
9160700004	FWC	2008/09/17	253916	12.7	9160800004	FWC	2008/09/20	1025948	12.9
9160900002	FWC	2008/09/21	519505	12.8	9161000002	FWC	2008/09/23	167731	12.7
9161300002	FWC	2008/09/29	189574	12.6	9161500004	FWC	2008/10/03	358285	12.6
9161600002	FWC	2008/10/05	1062545	12.6	9161900002	FWC	2008/10/11	268946	13.2
9162100003	FWC	2008/10/15	617166	12.8	9163100002	FWC	2008/11/04	341052	12.6
9164900002	FWC	2008/12/10	450612	12.9	9164900003	FWC	2008/12/10	536479	12.8
9165500004	FWC	2008/12/22	408866	12.8	9166200003	FWC	2009/01/05	175344	12.7
9168100003	FWC	2009/02/12	260532	13.6	9169500002	FWC	2009/03/12	245522	13.2
9169600003	FWC	2009/03/14	273413	13.1	9169700004	FWC	2009/03/16	591747	13.2
9169800002	FWC	2009/03/17	725286	13.4	9169900004	FWC	2009/03/20	804165	13.4
9170200002	FWC	2009/03/25	362767	13.3	9170300002	FWC	2009/03/28	816309	13.4
9170500003	FWC	2009/03/31	700702	13.6	9171000002	FWC	2009/04/10	926909	13.5
9171000003	FWC	2009/04/11	450835	13.3	9171100004	FWC	2009/04/13	225876	13.2
9171600003	FWC	2009/04/23	756501	13.6	9172300002	FWC	2009/05/06	720995	13.4
9173400002	FWC	2009/05/29	1180658	13.7	9175700002	FWC	2009/07/14	826809	14.0

## Continuation of Table 1

(1)	(2)	(3)	(4)	(5)	(1)	(2)	(3)	(4)	(5)
9176600004	FWC	2009/08/01	346700	13.6	9176700003	FWC	2009/08/03	472923	14.1
9176800004	FWC	2009/08/05	300521	13.8	9176900004	FWC	2009/08/07	285291	13.4
9177600004	FWC	2009/08/20	603084	13.5	9178100003	FWC	2009/08/31	309352	13.6
9179300002	FWC	2009/09/23	591640	13.6	9180400003	FWC	2009/10/15	454489	13.8
9180700003	FWC	2009/10/21	744110	14.0	9181300003	FWC	2009/11/02	951097	13.9
9181400002	FWC	2009/11/04	209205	14.0	9181500003	FWC	2009/11/07	832036	13.9
9181700003	FWC	2009/11/11	415449	14.0	9181900003	FWC	2009/11/15	740379	14.0
9182100003	FWC	2009/11/18	928535	14.2	9182200003	FWC	2009/11/21	848690	14.0
9182500003	FWC	2009/11/26	534366	14.0	9185700003	FWC	2010/01/29	267074	13.6
9187200003	FWC	2010/02/28	405573	13.5	9187300003	FWC	2010/03/02	591189	13.4
9187400002	FWC	2010/03/04	751984	13.1	9187400003	FWC	2010/03/04	443820	13.2
9188300003	FWC	2010/03/22	192226	12.7	9189200004	FWC	2010/04/09	668569	12.2
9190100002	FWC	2010/04/27	882667	12.5	9190400003	FWC	2010/05/03	244769	12.5
9190600003	FWC	2010/05/07	409138	12.2	9191000002	FWC	2010/05/15	1134923	12.7
9191100005	FWC	2010/05/17	549655	12.8	9191300004	FWC	2010/05/21	877200	12.3
9191600003	FWC	2010/05/27	498337	12.4	9191700004	FWC	2010/05/29	1010112	11.9
9191800002	FWC	2010/05/31	1010659	12.4	9192100003	FWC	2010/06/06	397557	12.0
9193100002	FWC	2010/06/26	377031	12.0	9193200002	FWC	2010/06/28	545220	12.3
9194500007	FWC	2010/07/24	380832	12.4	9194800004	FWC	2010/07/29	625569	12.0
9195000003	FWC	2010/08/02	658117	12.2	9196600002	FWC	2010/09/04	913746	12.2
9196900002	FWC	2010/09/09	220959	12.6	9197000002	FWC	2010/09/11	929152	12.1
9197500003	FWC	2010/09/21	399390	11.7	9198100002	FWC	2010/10/03	390516	12.0
9198300002	FWC	2010/10/07	716620	11.8	9198400003	FWC	2010/10/10	443393	12.2
9198700006	FWC	2010/10/16	192493	12.1	9198900002	FWC	2010/10/19	320276	12.0
9198900004	FWC	2010/10/20	780709	11.9	9199200004	FWC	2010/10/25	185636	11.8
9199500004	FWC	2010/10/31	336063	11.1	9200100005	FWC	2010/11/12	563142	11.8
9200200002	FWC	2010/11/14	568866	11.6	9200400003	FWC	2010/11/18	373046	11.5
9200900003	FWC	2010/11/28	307234	11.6	9201300003	FWC	2010/12/07	730248	11.6
9201400003	FWC	2010/12/08	292366	11.8	9201500003	FWC	2010/12/10	1144808	11.7
9202100003	FWC	2010/12/22	330234	11.6	9202900002	FWC	2011/01/06	741634	11.6
9204700002	FWC	2011/02/12	282536	11.7	9205700003	FWC	2011/03/04	1121528	11.4
9207100003	FWC	2011/03/31	463037	10.8	9207600004	FWC	2011/04/11	299694	10.8
9207700003	FWC	2011/04/13	612780	10.2	9208100004	FWC	2011/04/21	1051383	10.5
9208400003	FWC	2011/04/27	942753	10.8	9209500004	FWC	2011/05/19	561570	10.9
9209600002	FWC	2011/05/20	1155921	10.9	9209800002	FWC	2011/05/24	957568	11.0
9210100003	FWC	2011/05/31	744293	10.4	9210700004	FWC	2011/06/12	696953	10.5
9211600002	FWC	2011/06/29	1047641	9.8	9211700002	FWC	2011/07/01	376951	10.0
9214900004	FWC	2011/09/04	249888	10.3	9218200004	FWC	2011/11/08	454187	10.3
9218300002	FWC	2011/11/10	435766	10.2	9223300002	FWC	2012/02/18	935851	9.9
9225900003	FWC	2012/04/10	560296	9.7	9226100002	FWC	2012/04/14	1035930	9.9
9226400004	FWC	2012/04/20	464484	10.3	9227500006	FWC	2012/05/12	611512	9.7
9227600002	FWC	2012/05/13	394875	9.6	9229000002	FWC	2012/06/10	324826	9.0
9229600003	FWC	2012/06/22	323646	9.3	9229700003	FWC	2012/06/25	267659	9.8
9229900003	FWC	2012/06/28	265961	9.7	9230100004	FWC	2012/07/03	260672	9.5
9231800002	FWC	2012/08/05	673050	8.1	9232100004	FWC	2012/08/11	1199939	8.3
9233000003	FWC	2012/08/29	403990	8.7	9233900005	FWC	2012/09/16	782485	8.7
9236300002	FWC	2012/11/03	669150	8.7	9236600002	FWC	2012/11/09	1042098	9.0
9236700002	FWC	2012/11/10	1144366	8.9	9236900002	FWC	2012/11/14	865821	8.5
9238200002	FWC	2012/12/10	1038779	8.7	9238700004	FWC	2012/12/21	766697	8.6
9239400003	FWC	2013/01/04	678821	9.0	9240900002	FWC	2013/02/03	595050	9.3
9241200002	FWC	2013/02/08	371796	8.9	9241500002	FWC	2013/02/14	944903	9.3
9241600002	FWC	2013/02/16	196163	9.6	9242200003	FWC	2013/03/01	359328	9.1

## Continuation of Table 1

(1)	(2)	(3)	(4)	(5)	(1)	(2)	(3)	(4)	(5)
9242700002	FWC	2013/03/11	401728	9.5	9245700004	FWC	2013/05/10	405283	8.9
9247900002	FWC	2013/06/22	182171	7.8	9248700002	FWC	2013/07/08	216005	8.1
9248900002	FWC	2013/07/12	425182	7.5	9248900003	FWC	2013/07/12	640578	7.6
9249100002	FWC	2013/07/16	1189396	7.6	9249300002	FWC	2013/07/20	1106856	8.1
9249400002	FWC	2013/07/22	603515	8.2	9249500003	FWC	2013/07/25	1073203	8.2
9249600002	FWC	2013/07/26	614271	8.2	9249700002	FWC	2013/07/28	615427	8.1
9249800002	FWC	2013/07/30	302452	7.8	9249900002	FWC	2013/08/01	708997	7.9
9254500004	FWC	2013/11/01	723226	7.9	9254600004	FWC	2013/11/03	830218	8.0
9256500002	FWC	2013/12/11	1028960	7.6	9256600002	FWC	2013/12/13	764499	7.8
9257300002	FWC	2013/12/26	274812	7.7	9258700002	FWC	2014/01/24	751265	7.8
9258800002	FWC	2014/01/26	557815	7.7	9259300002	FWC	2014/02/05	1018256	7.6
9261200003	FWC	2014/03/15	950946	7.2	9261600002	Med	2014/03/22	526843	7.7
9261700002	Med	2014/03/24	918132	7.7	9262500003	FWC	2014/04/10	1046692	7.7
9263300002	FWC	2014/04/25	271099	7.5	9264200002	FWC	2014/05/13	219010	7.9
9264400003	FWC	2014/05/17	737024	8.1	9265000003	FWC	2014/05/29	908458	7.8
9265500003	FWC	2014/06/09	396031	7.8	9266200002	FWC	2014/06/22	276761	7.4
9266700002	FWC	2014/07/02	531491	7.7	9267800004	FWC	2014/07/24	800161	8.1
9268600003	FWC	2014/08/09	1139448	7.8	9268900002	FWC	2014/08/15	993992	8.1
9269100003	FWC	2014/08/19	219321	8.4	9269300002	FWC	2014/08/23	769649	8.3
9270200002	FWC	2014/09/09	508512	8.1	9272200003	FWC	2014/10/20	689469	9.0
9272300003	FWC	2014/10/22	316186	8.9	9272400004	FWC	2014/10/24	1093791	8.3
9273200003	FWC	2014/11/09	842060	8.2	9273400004	FWC	2014/11/13	1160736	8.2
9274300003	FWC	2014/12/01	1002277	8.4	9274700002	FWC	2014/12/09	1008580	8.0
9275600002	FWC	2014/12/27	1109659	7.6	9275900004	FWC	2015/01/02	1066102	7.7
9276000005	FWC	2015/01/04	1046142	7.9	9276100002	FWC	2015/01/05	167170	7.9
9276400002	FWC	2015/01/11	492080	8.5	9276600002	FWC	2015/01/16	668181	8.8
9276600003	FWC	2015/01/16	611061	8.5	9276700003	FWC	2015/01/18	828185	8.6
9278000004	FWC	2015/02/13	607387	8.4	9278900002	FWC	2015/03/03	703201	7.8
9280600003	FWC	2015/04/06	349926	7.9	9281000002	FWC	2015/04/13	552695	7.5
9281200003	FWC	2015/04/18	637549	7.5	9281300003	FWC	2015/04/20	384110	7.6
9285000003	FWC	2015/07/02	948373	8.6	9285400002	FWC	2015/07/10	176059	9.0
9285400003	FWC	2015/07/10	559730	8.5	9285600002	FWC	2015/07/14	173366	8.4
9285700003	FWC	2015/07/16	669302	8.5	9288200003	FWC	2015/09/05	191254	9.0
9289500004	FWC	2015/09/30	305504	9.0	9289800002	FWC	2015/10/06	200066	8.8
9290800002	FWC	2015/10/26	608146	8.8	9291000004	FWC	2015/10/30	920331	9.3
9291100003	FWC	2015/11/01	529684	9.3	9291500002	FWC	2015/11/08	181708	8.7
9291600003	FWC	2015/11/11	491658	8.5	9291600004	FWC	2015/11/11	530926	8.6
9291700002	FWC	2015/11/13	272614	8.6	9291800002	FWC	2015/11/15	867688	8.9
9291900002	FWC	2015/11/17	470589	9.0	9292200002	FWC	2015/11/23	921948	9.2
9292300003	FWC	2015/11/25	579247	9.7	9292400005	FWC	2015/11/27	624384	9.5
9293100002	FWC	2015/12/11	1118775	8.9	9293400002	FWC	2015/12/16	196288	9.2
9293500002	FWC	2015/12/18	213549	9.4	9293700002	FWC	2015/12/22	844385	9.5
9294700014	FWC	2016/01/12	319966	9.4	9294800004	FWC	2016/01/14	282728	9.8
9294900005	FWC	2016/01/16	710342	9.7	9295700004	Med	2016/02/01	305377	10.2
9296400004	Med	2016/02/15	191602	10.2	9299500002	Med	2016/04/16	297925	10.1
9299500003	Med	2016/04/16	625763	10.3	9299800004	Med	2016/04/23	164251	10.2
9300500002	Med	2016/05/06	236379	10.1	9300500004	Med	2016/05/06	1016731	10.7
9300900004	Med	2016/05/15	504497	10.8	9301000003	Med	2016/05/16	418266	10.8
9301200005	Med	2016/05/21	1170913	10.2	9301400002	Med	2016/05/24	197225	10.4
9301500005	Med	2016/05/27	348926	10.8	9302200006	Med	2016/06/10	676012	11.1
9302400003	Med	2016/06/13	578355	10.9	9302900003	Med	2016/06/24	173836	10.4
9303100002	Med	2016/06/27	320084	10.5	9303200005	Med	2016/06/29	718162	10.9



## Continuation of Table 1

(1)	(2)	(3)	(4)	(5)	(1)	(2)	(3)	(4)	(5)
9304200004	Med	2016/07/19	985842	10.4	9304200005	Med	2016/07/19	244540	11.0
9305600003	FWC	2016/08/16	767599	10.8	9305600004	FWC	2016/08/16	807778	11.0
9305700003	FWC	2016/08/18	943507	10.7	9305700005	FWC	2016/08/18	352480	11.0
9305800002	FWC	2016/08/20	843569	10.9	9306300003	FWC	2016/08/30	405606	11.8
9306400004	FWC	2016/09/01	1102454	11.2	9307500002	FWC	2016/09/22	438809	11.6
9307800002	FWC	2016/09/28	285355	11.3	9307900004	FWC	2016/10/01	546743	10.8
9307900005	FWC	2016/10/01	1142451	11.1	9308100004	FWC	2016/10/05	641869	11.4
9308100005	FWC	2016/10/05	442307	11.3	9308700003	FWC	2016/10/17	557726	11.3
9309200003	FWC	2016/10/27	446345	11.4	9309500002	FWC	2016/11/01	518427	11.5
9309900002	FWC	2016/11/10	804167	11.8	9310200004	FWC	2016/11/16	830683	12.0
9311100002	FWC	2016/12/03	274180	11.9	9311100005	FWC	2016/12/04	883407	12.2
9311600004	FWC	2016/12/14	427108	12.4	9312000002	FWC	2016/12/22	164444	11.8
9312000003	FWC	2016/12/22	542822	11.9	9312000004	FWC	2016/12/22	358101	11.8
9313500002	FWC	2017/01/20	800550	12.3	9315100002	FWC	2017/02/22	267558	12.7
9316200002	FWC	2017/03/16	857240	12.9	9316200003	FWC	2017/03/16	273717	12.5
9317200002	FWC	2017/04/04	271624	11.9	9319100004	FWC	2017/05/13	725326	12.9
9321200004	FWC	2017/06/23	654216	13.1	9321700003	FWC	2017/07/03	348437	12.2
9322400005	FWC	2017/07/18	768957	12.0	9323600003	FWC	2017/08/10	402662	12.3
9324200003	FWC	2017/08/22	354198	11.4	9324400004	FWC	2017/08/26	1115586	11.8
9325500002	FWC	2017/09/17	143721	11.2	9327000002	FWC	2017/10/17	796044	11.8
9327600004	FWC	2017/10/29	179335	12.0	9328000003	FWC	2017/11/06	896198	12.2
9328400002	FWC	2017/11/13	309746	12.1	9328700006	FWC	2017/11/20	820495	12.7
9329500002	FWC	2017/12/05	145165	12.6	9330400003	FWC	2017/12/24	140402	12.8
9331600004	FWC	2018/01/16	342229	13.1	9333900003	FWC	2018/03/03	241550	13.2
9334400004	FWC	2018/03/14	1109132	13.4	9336200003	FWC	2018/04/18	250776	13.3
9336800004	Med	2018/05/01	138831	13.1	9337300006	FWC	2018/05/10	290849	13.0
9337400003	FWC	2018/05/13	310356	13.6	9337500004	FWC	2018/05/15	249747	13.5
9337700003	FWC	2018/05/18	172260	13.1	9338000002	FWC	2018/05/24	396609	12.9
9338400002	FWC	2018/06/01	713152	13.7	9339200003	FWC	2018/06/17	585428	13.9
9339700003	FWC	2018/06/28	669044	12.7	9341100003	FWC	2018/07/26	611272	13.3
9342500003	FWC	2018/08/22	390765	13.6	9342700002	FWC	2018/08/26	319624	13.6
9342900002	FWC	2018/08/30	739933	13.4	9345300003	FWC	2018/10/17	315345	13.6
9345900003	FWC	2018/10/29	608707	13.8	9346400002	FWC	2018/11/08	742179	13.5
9346500002	FWC	2018/11/10	1043936	13.3	9346700003	FWC	2018/11/14	336528	13.2
9347100007	FWC	2018/11/22	958020	13.8	9347100008	FWC	2018/11/22	298778	14.0
9347300003	FWC	2018/11/25	319035	13.6	9348600002	FWC	2018/12/21	716599	13.8
9352800003	FWC	2019/03/15	240520	13.8	9354500004	FWC	2019/04/18	652828	14.0
9354900002	FWC	2019/04/26	197567	13.9	9355400007	FWC	2019/05/06	428732	14.0
9355500002	FWC	2019/05/09	577381	13.6	9355600002	FWC	2019/05/11	577058	13.2
9356200004	FWC	2019/05/22	421150	13.6	9358300002	FWC	2019/07/03	1026272	13.9
9358900003	FWC	2019/07/15	249014	13.8	9359200002	FWC	2019/07/21	241940	14.4
9359200004	FWC	2019/07/21	522385	14.2	9359600003	FWC	2019/07/30	998555	14.0
9359800003	FWC	2019/08/02	1149916	14.1	9360200002	FWC	2019/08/10	540230	13.8
9360600002	FWC	2019/08/18	580090	14.1	9361100002	FWC	2019/08/28	437059	14.0
9362400002	FWC	2019/09/23	631360	14.4	9362600002	FWC	2019/09/26	174873	14.1
9362700005	FWC	2019/09/29	380936	14.0	9363300002	FWC	2019/10/10	1008347	14.2
9363500002	FWC	2019/10/15	554776	14.3	9364100003	FWC	2019/10/27	957774	13.9
9364200003	FWC	2019/10/29	685418	14.1	9364200004	FWC	2019/10/29	269886	14.1
9364300004	FWC	2019/10/31	614396	14.3	9364400003	FWC	2019/11/02	594039	13.8
9364600002	FWC	2019/11/05	605596	14.1	9364600003	FWC	2019/11/06	412003	14.3
9364700002	FWC	2019/11/07	1201808	14.3	9364800004	FWC	2019/11/10	428537	14.5
9365200002	FWC	2019/11/17	698482	14.2	9365200004	FWC	2019/11/18	393143	14.4



## Continuation of Table 1

(1)	(2)	(3)	(4)	(5)	(1)	(2)	(3)	(4)	(5)
9365300002	FWC	2019/11/19	805944	14.3	9366100004	FWC	2019/12/06	203332	14.4
9366300002	FWC	2019/12/09	685067	14.3	9366400003	FWC	2019/12/12	182759	14.2
9368200002	FWC	2020/01/16	565202	14.2	9368300003	FWC	2020/01/19	346330	14.4
9369800002	FWC	2020/02/17	257636	14.6	9371100002	FWC	2020/03/15	336133	14.4
9372000002	FWC	2020/04/01	282765	14.4	9372300003	FWC	2020/04/07	589725	14.8
9372500002	FWC	2020/04/11	231638	14.5	9373200002	FWC	2020/04/25	176451	14.8
9373600003	FWC	2020/05/03	533969	14.1	9374300002	FWC	2020/05/18	808119	14.5
9375000002	FWC	2020/06/01	837827	14.5	9376100003	FWC	2020/06/22	546639	14.8
9377600003	FWC	2020/07/22	492169	14.9	9380900002	FWC	2020/09/25	1045963	13.9
9381100002	FWC	2020/09/30	232651	13.8	9382600002	FWC	2020/10/29	1121726	14.1
9382600004	FWC	2020/10/30	333598	14.5	9383600002	FWC	2020/11/18	853611	14.4
9383900002	FWC	2020/11/24	260636	14.0	9384200002	FWC	2020/12/01	792131	15.1
9384300002	FWC	2020/12/03	983104	14.6	9385000002	FWC	2020/12/16	183055	14.2
9385200002	FWC	2020/12/20	341423	13.7	9385300003	FWC	2020/12/22	1092919	13.8
9385400003	FWC	2020/12/25	283229	14.0	9385900003	FWC	2021/01/03	192986	13.9
9386100003	FWC	2021/01/08	634424	13.9	9386300004	FWC	2021/01/12	1017226	13.4
9389400003	FWC	2021/03/15	836867	13.7	9389500003	FWC	2021/03/16	215495	13.8
9389600003	FWC	2021/03/18	191737	13.8	9389900003	FWC	2021/03/24	190492	13.9
9390000004	FWC	2021/03/26	177079	13.2	9390000006	FWC	2021/03/27	169555	13.7
9390300003	FWC	2021/04/02	180241	14.2	9391300003	FWC	2021/04/21	212539	13.3
9391400004	FWC	2021/04/23	187862	14.2	9391500002	FWC	2021/04/26	301412	13.9
9392100002	FWC	2021/05/08	468470	13.8	9392200002	FWC	2021/05/09	941516	13.6
9392400002	FWC	2021/05/13	855626	13.7	9392600002	FWC	2021/05/17	822558	13.7
9392900002	FWC	2021/05/23	262773	14.4	9393000002	FWC	2021/05/25	581991	14.4
9393100003	FWC	2021/05/27	285148	13.9	9393300002	FWC	2021/05/31	1198966	14.3
9393800003	FWC	2021/06/11	871319	14.0	9394500003	FWC	2021/06/24	640088	14.3
9395000003	FWC	2021/07/04	239706	14.4	9395900002	FWC	2021/07/22	353774	14.1
9395900003	FWC	2021/07/22	1172248	14.0	9396900002	FWC	2021/08/10	991042	14.0
9396900003	FWC	2021/08/11	987147	14.1	9397000002	FWC	2021/08/12	990990	13.9
9397000003	FWC	2021/08/13	977884	14.0	9397100002	FWC	2021/08/14	332194	14.4
9397100005	FWC	2021/08/15	259719	14.3	9397200002	FWC	2021/08/16	213972	14.1
9397200005	FWC	2021/08/17	238072	14.2	9397300002	FWC	2021/08/18	285510	14.5
9397300005	FWC	2021/08/19	768307	14.7	9399300003	FWC	2021/09/28	385239	13.4
9400500003	FWC	2021/10/22	210041	13.8	9401500004	FWC	2021/11/11	413549	14.1
9401900002	FWC	2021/11/19	953019	13.5	9402300003	FWC	2021/11/26	1012097	13.9
9403300002	FWC	2021/12/16	368013	13.5	9403400003	FWC	2021/12/19	178165	13.5
9403500002	FWC	2021/12/20	558016	13.8	9403600003	FWC	2021/12/22	411436	13.4
9404500002	FWC	2022/01/09	558999	13.5	9404900002	FWC	2022/01/17	1169373	13.5
9405400002	FWC	2022/01/27	343044	13.3	9405500002	FWC	2022/01/29	339128	13.3
9405600002	FWC	2022/01/31	809146	13.7	9405700002	FWC	2022/02/02	997842	13.0
9405800002	FWC	2022/02/04	298712	13.3	9405900002	FWC	2022/02/06	926728	13.2
9406000002	FWC	2022/02/09	557540	13.6	9406600003	FWC	2022/02/20	691895	13.5
9406700004	FWC	2022/02/23	439510	12.8	9406900002	FWC	2022/02/26	998593	13.2
9408100003	FWC	2022/03/22	462685	13.3	9408200003	FWC	2022/03/24	484379	13.2
9409500002	FWC	2022/04/19	907558	13.1	9409800003	FWC	2022/04/25	496551	12.4
9410500004	FWC	2022/05/10	374369	11.9	9410800007	FWC	2022/05/15	382594	12.8
9411400002	FWC	2022/05/28	236706	12.1	9414500002	FWC	2022/07/28	1204891	10.5
9414600004	FWC	2022/07/30	173260	10.9	9416000002	FWC	2022/08/27	185959	10.2
9417500002	FWC	2022/09/25	524943	10.3	9417600002	FWC	2022/09/27	776095	9.7
9420200002	FWC	2022/11/18	328076	10.6	9420600005	FWC	2022/11/27	254437	10.2
9423600005	FWC	2023/01/26	281947	9.5	9423900005	FWC	2023/02/01	794129	9.7
9424200002	FWC	2023/02/06	499062	9.9	9424600003	FWC	2023/02/15	839094	9.4

Continuation of Table 1

(1)	(2)	(3)	(4)	(5)	(1)	(2)	(3)	(4)	(5)
9427400002	FWC	2023/04/11	412498	9.1	9427800002	FWC	2023/04/19	175099	8.6
9427900003	FWC	2023/04/22	893408	8.8	9430300003	FWC	2023/06/08	459575	8.5
9431100005	FWC	2023/06/24	328207	8.5	9431400003	FWC	2023/06/30	243570	8.1
9433900003	FWC	2023/08/19	404258	7.4	9435600002	FWC	2023/09/22	522256	7.0
9436200002	FWC	2023/10/03	1164979	7.3	9437100002	FWC	2023/10/21	236664	7.0